Comput. Mech. (2007) 39: 537–554
DOI 10.1007/s00466-006-0057-6

ORIGINAL PAPER

Y. Li · G.R. Liu · M.T. Luan · K.Y. Dai
Z.H. Zhong · G.Y. Li · X. Han

Contact analysis for solids based on linearly conforming radial point interpolation method

Received: 6 September 2005 / Accepted: 3 February 2006 / Published online: 29 March 2006

Abstract To simulate the contact nonlinearity in 2D solid problems, a contact analysis approach is formulated using incremental form of the subdomain parametric variational principle (SPVP). The formulation is based on a linearly conforming radial point interpolation method (LC-RPIM) using nodal integration technique. Contact interface equations are also presented using a modified Coulomb frictional contact model and discretized by contact point-pairs. In the present approach, the global discretized system equations are transformed into a standard linear complementarity problem (LCP) that can be solved readily using the Lemke method. The present approach can simulate various contact behaviors including bonding/debonding, contacting/departing, and sticking/slipping. An intensive numerical study is performed to validate the proposed method via comparison with the ABAQUS® and to investigate the effects of the various parameters used in computations. These parameters include normal and tangential adhesions, frictional coefficient, nodal density, the dimension of local nodal support domain, nodal irregularity, shape parameters used in the radial basis function and the external load. The numerical results have demonstrated that the present approach is accurate and stable for contact analysis of 2D solids.

Y. Li · G.R. Liu (✉) · K.Y. Dai
Centre for Advanced Computations in Engineering Science,
Department of Mechanical Engineering,
National University of Singapore,
10 Kent Ridge Crescent, Singapore,
119260, Singapore
E-mail: mpeliugr@nus.edu.sg

Y. Li · M.T. Luan
School of Civil and hydraulic Engineering,
Dalian University of Technology,
2 Linggong Road, Dalian,
116024, P. R. China

Z.H. Zhong · G.Y. Li · X. Han
Key Laboratory of Advanced Technology
for Vehicle Body Design & Manufacture,
M.O.E, Hunan University, Changsha,
410082, P. R. China

Keywords Frictional contact · Contact interface model · Meshfree method · Interpolation function · Gradient smoothing · Parametric variational principle

1 Introductioin

Contact problems are very important in many fields such as mechanical and civil engineering [1, 2], which have the characteristics of geometric and material discontinuity at the contact interface rather than the usual continuity property in solid mechanics. The strong nonlinearity is difficult to solve by the analytical method for problems of complex boundaries, and hence numerical methods are needed [1–27]. When handling contact constraints or behaviors, we mainly use penalty method [1–6, 22, 24, 25], Lagrangian multiplier and augmented lagrangian method [5–11, 19], mathematical programming [11–13, 26, 27], and other methods [13–18, 20, 21, 23]. Note that all of these methods are based on "element" or "mesh" and hence may give rise to problems related to mesh distortions.

Meshfree methods or element free methods have been developed in recent years, such as the smooth particle hydrodynamics (SPH) method that uses integral representation of a function and particle approximation to create discretized system equations [28–33], the element-free Galerkin (EFG) method [34–36] that uses moving least squares (MLS) approximation and the Galerkin weak form, the reproducing kernel particle method (RKPM) that ensures the certain degree of consistency of the integral approximation by modifying integral kernel function [37], the meshless local Petrov–Galerkin (MLPG) that uses the local Petrov-Galerkin weak form [38–40], the point interpolation method (PIM) and radial point interpolation method (RPIM) [41–45]. Detailed descriptions and discussions on these meshfree methods can be found in, for example [28, 29]. The RPIM has the following advantages:

(1) The shape function has the Kronecker delta property.
(2) The moment matrix used in constructing shape functions is always invertible for irregular nodes.

(3) The linear field can be exactly reproduced using RPIM shape functions augmented with linear polynomials.

However, background cells must be used for Gaussian integration of the Galerkin weak form. In addition, the RPIM is not conforming unless the constrainted weak form is used [28]. Hence, shape parameters need to be properly chosen to control the inconformability, in order to obtain accurate results [28]. To overcome these disadvantages, a linearly conforming radial point interpolation method (LC-RPIM) is recently developed [46, 47] through gradient smoothing and nodal integration by means of the stabilized conforming nodal integration (SCNI) techniques [48, 49]. The LC-RPIM can exactly pass the standard linear patch test, which is very stable, accurate and efficient as demonstrated in intensive case studies [47].

To date, very few contact analyses use meshfree methods [50, 51] in literature to the best of our knowledge. In this paper, we confine our attention to static contact analysis of solid systems composed of rigid and/or deformable solids in two dimensions, which is formulated in incremental form through the subdomain parametric variational principle based on the LC-RPIM and contact interface equations using a modified Coulomb frictional contact model.

This paper is organized as follows. Section 2 reviews briefly the procedure of creating shape functions with the Kronecker delta function property that is very important for contact analysis and gradient smoothing procedure in the LC-RPIM. Section 3 describes a contact interface model and its discretization. Section 4 gives out first the parametric variational principle in the incremental form of boundary value problems for a solid, then derives the corresponding discrete system equations, and finally those equations are transformed into a set of equations of a standard linear complementarity problem (LCP). Section 5 presents a number of numerical examples to validate the proposed contact analysis approach, by comparison with ABAQUS® and analytical formulae. Some conclusions are drawn in the last section.

2 Displacement interpolation and gradient smoothing in LC-RPIM

The shape functions used in the LC-RPIM are created through interpolation using local nodes and radial and polynomial basis functions. Such an interpolation is often used by many researchers for curve or surface fitting and function approximation [52, 53]. The gradient of the field function (displacement) at a node is smoothed through an integration over the local domain such as the Voronoi cell [47, 48], which satisfies the Gaussian theorem [54] and subsequently guarantees the exact linear displacement solution [46, 47]. The procedure of constructing RPIM shape functions of displacement and gradient smoothing in the LC-RPIM is briefed as follows.

2.1 Shape function of displacement interpolation

A field function $u(\boldsymbol{x})$ that is a component of the displacement can be approximated using both radial and polynomial basis functions in the form of

$$u(\boldsymbol{x}) = \sum_{i}^{n} R_i(\boldsymbol{x}) a_i + \sum_{j}^{m} P_j(\boldsymbol{x}) b_j = \boldsymbol{R}^{\mathrm{T}}(\boldsymbol{x})\boldsymbol{a} + \boldsymbol{P}^{\mathrm{T}}(\boldsymbol{x})\boldsymbol{b} \tag{2.1}$$

where n is the number of field nodes in the local support domain for point $\boldsymbol{x}$; the vector of $\boldsymbol{R}(\boldsymbol{x}) = [R_1(\boldsymbol{x}), \ldots, R_k(\boldsymbol{x}), \ldots, R_{\mathrm{n}}(\boldsymbol{x})]^{\mathrm{T}}$ is composed of radial basis functions $R_k(\boldsymbol{x}) = R(r_k)$, here $r_k = \left[(x_k - x)^2 + (y_k - y)^2\right]^{\frac{1}{2}}$ is a distance between the point $\boldsymbol{x}$ and field node $\boldsymbol{x}_k$; $\boldsymbol{P}(\boldsymbol{x}) = [P_1(\boldsymbol{x}), P_2(\boldsymbol{x}), \ldots, P_m(\boldsymbol{x})]^{\mathrm{T}}$ is the vector of polynomial basis functions in 2D space $\boldsymbol{x}^{\mathrm{T}} = [x, y]$ which has the form $\boldsymbol{P}(\boldsymbol{x}) = \left[1, x, y, x^2, xy, y^2, \ldots\right]^{\mathrm{T}}$, and m is the number of terms of the polynomial basis functions. For example, when $\boldsymbol{P}(\boldsymbol{x}) = [1, x, y]^{\mathrm{T}}$ is used, we have $m = 3$. $\boldsymbol{a} = [a_1, a_2, \ldots, a_{\mathrm{n}}]^{\mathrm{T}}$ and $\boldsymbol{b} = [b_1, b_2, \ldots, b_m]^{\mathrm{T}}$ are, respectively, coefficients for $\boldsymbol{R}(\boldsymbol{x})$ and $\boldsymbol{P}(\boldsymbol{x})$. The radial basis functions are usually used to create a nonsingular moment matrix, and the polynomial basis functions are used to ensure the polynomial field reproducibility of the generated shape functions [28, 29].

The coefficient vectors $\boldsymbol{a}$ and $\boldsymbol{b}$ are determined by enforcing Eq. (2.1) to be satisfied at all the n field nodes within the local support domain. Following the lengthy but straightforward procedure given by [28, 47], we can arrive at

$$u(\boldsymbol{x}) = \boldsymbol{N}(\boldsymbol{x})\boldsymbol{U}_{\mathrm{s}} \tag{2.2}$$

where $\boldsymbol{U}_{\mathrm{s}} = [u_1, u_2, \ldots, u_{\mathrm{n}}]^{\mathrm{T}}$ is a vector of nodal displacements for nodes in the local support domain, and $\boldsymbol{N}(\boldsymbol{x}) = [N_1(\boldsymbol{x}), \ldots, N_k(\boldsymbol{x}), \ldots, N_{\mathrm{n}}(\boldsymbol{x})]$ contains RPIM shape functions for the n local nodes in which $N_k(\boldsymbol{x})$ is provided by

$$N_k(\boldsymbol{x}) = \sum_{i}^{n} R_i(\boldsymbol{x}) \boldsymbol{S}_{aik} + \sum_{j}^{m} P_j(\boldsymbol{x}) \boldsymbol{S}_{bjk} \tag{2.3}$$

where $\boldsymbol{S}_{aik}$ is the (i, k) entry of matrix $\boldsymbol{S}_a = \boldsymbol{R}_{\mathrm{M}}^{-1} - \boldsymbol{R}_{\mathrm{M}}^{-1}\boldsymbol{P}_{\mathrm{M}}\boldsymbol{S}_b$, and $\boldsymbol{S}_{bjk}$ is the (j, k) entry of matrix $\boldsymbol{S}_b = \left(\boldsymbol{P}_{\mathrm{M}}^{\mathrm{T}}\boldsymbol{R}_{\mathrm{M}}^{-1}\boldsymbol{P}_{\mathrm{M}}\right)^{-1}\boldsymbol{P}_{\mathrm{M}}^{\mathrm{T}}\boldsymbol{R}_{\mathrm{M}}^{-1}$. The moment matrices $\boldsymbol{R}_{\mathrm{M}}$ and $\boldsymbol{P}_{\mathrm{M}}$ are, respectively, consisted of row vectors $\boldsymbol{R}^{\mathrm{T}}(\boldsymbol{x}_i)$ and $\boldsymbol{P}^{\mathrm{T}}(\boldsymbol{x}_i)$ $(i = 1, 2, \ldots, n)$ [28, 29, 47].

The shape function $N_k(\boldsymbol{x})$ has simple gradient (or first derivative) such as

$$\nabla N_k(\boldsymbol{x}) = \begin{Bmatrix} \dfrac{\partial N_k(\boldsymbol{x})}{\partial x} \\ \dfrac{\partial N_k(\boldsymbol{x})}{\partial y} \end{Bmatrix} = \sum_{i}^{n} \frac{\partial R_i(\boldsymbol{x})}{\partial r_i} \frac{\boldsymbol{S}_{aik}}{r_i} \begin{Bmatrix} x - x_i \\ y - y_i \end{Bmatrix} + \sum_{j}^{m} \boldsymbol{S}_{bjk} \begin{Bmatrix} \dfrac{\partial P_j(\boldsymbol{x})}{\partial x} \\ \dfrac{\partial P_j(\boldsymbol{x})}{\partial y} \end{Bmatrix} \tag{2.4}$$

There are many types of radial basis functions (RBFs) [28, 29, 52, 53]. In the paper the standard multiquadrics radial basis function (MQ-RBF) with arbitrary real shape parameters is used [28, 55]:

$$R(r_i) = \left(r_i^2 + \alpha_c^2 d_c^2\right)^q \tag{2.5}$$

where d_c is a characteristic length that is related to nodal spacing in local support domain, which is usually the average nodal spacing for all the supporting nodes. For two dimensions it can be estimated using $d_c = \sqrt{A_s}/\left(\sqrt{n_s} - 1\right)$ [28]. Here A_s is an estimated area covered by the local support domain and n_s is the number of included nodes. α_c and q are two shape parameters for the MQ-RBF, which are real and needed to be determined by numerical tests [28].

2.2 Gradient smoothing

RPIM shape functions with linear consistency can be obtained by including complete linear polynomial basis functions ($m = 3$). However, the conventional RPIM may not be linearly conforming because of the inconformability in the weak form [46, 47]. So a smoothing operation to the gradient of the field function need to be performed [46–49]:

$$\nabla^h \boldsymbol{u}_i = \nabla^h \boldsymbol{u}(\boldsymbol{x}_i) = \int_{\Omega_i} \nabla \boldsymbol{u}(\boldsymbol{x}) \Phi(\boldsymbol{x} - \boldsymbol{x}_i) \mathrm{d}\Omega \tag{2.6}$$

where Φ is a smoothing function, Ω_i is the smoothing domain (such as Voronoi cell) of the ith field node and Γ_i is its boundary, as shown in Fig. 1.

Using integration by parts, the Eq. (2.6) may be rewritten as

$$\nabla^h \boldsymbol{u}_i = \int_{\Gamma_i} \boldsymbol{n}(\boldsymbol{x}) \boldsymbol{u}(\boldsymbol{x}) \Phi(\boldsymbol{x} - \boldsymbol{x}_i) \mathrm{d}\Gamma - \int_{\Omega_i} \boldsymbol{u}(\boldsymbol{x}) \nabla \Phi(\boldsymbol{x} - \boldsymbol{x}_i) \mathrm{d}\Omega \tag{2.7}$$

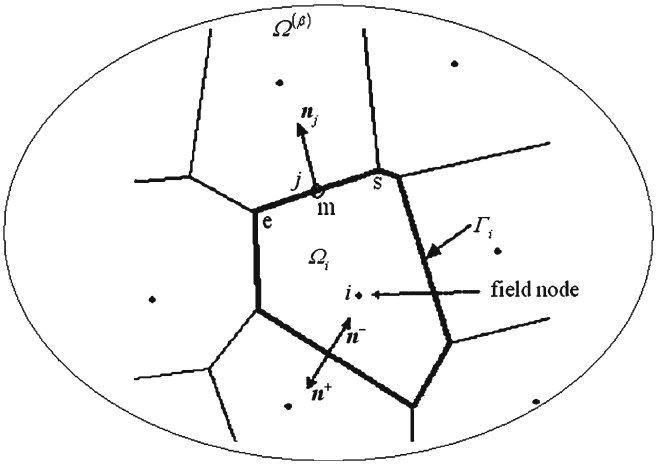

Fig. 1 Voronoi cell for a field node i in a subdomain $\Omega^{(\beta)}$ (bdoy β) of 2D

For simplicity, the following piecewise constant smoothing function is used:

$$\Phi(\boldsymbol{x} - \boldsymbol{x}_i) = \begin{cases} \dfrac{1}{A_i} & \boldsymbol{x} \in \Omega_i \\ 0 & \boldsymbol{x} \notin \Omega_i \end{cases} \tag{2.8}$$

where A_i is the area of the representative domain of the ith field node obtained from, for example, the Voronoi cell of node i as shown in Fig. 1.

Substituting Eq. (2.8) into Eq. (2.7), we obtain

$$\nabla^h \boldsymbol{u}_i = \frac{1}{A_i} \int_{\Gamma_i} \boldsymbol{n}(\boldsymbol{x}) \boldsymbol{u}(\boldsymbol{x}) \mathrm{d}\Gamma \tag{2.9}$$

Using the trapezoidal integration with three points on each edge of the Voronoi cell for field node i, Eq. (2.9) can then be given in form of

$$\nabla^h \boldsymbol{u}_i = \frac{1}{4A_i} \sum_{j=1}^{n_i^{\mathrm{VE}}} L_j^{\mathrm{VE}} \boldsymbol{n}_j \left(\boldsymbol{u}\left(\boldsymbol{x}_j^{\mathrm{s}}\right) + 2\boldsymbol{u}\left(\boldsymbol{x}_j^{\mathrm{m}}\right) + \boldsymbol{u}\left(\boldsymbol{x}_j^{\mathrm{e}}\right)\right) \tag{2.10}$$

where n_i^{VE} is the number of the edges of the Voronoi cell associated with the ith node, L_j^{VE} and $\boldsymbol{n}_j$ are the length and outward normal vector of the jth Voronoi edge for field node i. $\boldsymbol{u}\left(\boldsymbol{x}_j^{\mathrm{s}}\right)$, $\boldsymbol{u}\left(\boldsymbol{x}_j^{\mathrm{m}}\right)$ and $\boldsymbol{u}\left(\boldsymbol{x}_j^{\mathrm{e}}\right)$ are, respectively, the displacements at the start, middle and end points of the jth Voronoi edge in counterclockwise direction, as shown in Fig. 1.

Using the RPIM shape functions ($m = 3$), the average smoothed gradient matrix $\bar{\boldsymbol{B}}_i$ for the ith field node can be given as

$$\bar{\boldsymbol{B}}_i = \bar{\boldsymbol{B}}(\boldsymbol{x}_i) = \frac{1}{4A_i} \sum_{j=1}^{n_i^{\mathrm{VE}}} L_j^{\mathrm{VE}} \boldsymbol{n}_j \left(\boldsymbol{N}\left(\boldsymbol{x}_j^{s}\right) + 2\boldsymbol{N}\left(\boldsymbol{x}_j^{\mathrm{m}}\right) + \boldsymbol{N}\left(\boldsymbol{x}_j^{\mathrm{e}}\right)\right) \tag{2.11}$$

It has been shown that the use of Eq. (2.11) to compute the strain matrix is sufficient to obtain exact linear solution for methods based on the Galerkin weak form [46–49, 56].

3 Contact interface equations

For simplicity, we consider surface-to-surface contact under the small deformation here. This section describes briefly a modified Coulomb frictional contact model, then its discretized form is given out in incremental form using contact point-pairs together with the RPIM shape functions for displacement interpolation.

3.1 Contact interface model

It is very important to accurately represent the behavior of a contact interface in a solid system. For example, Fig. 2

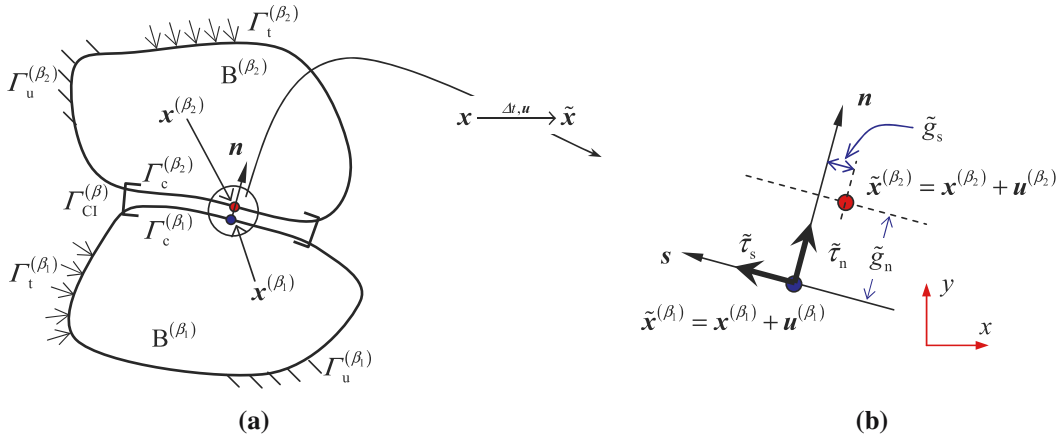

Fig. 2 A contact interface between arbitrary two bodies β_1 and β_2. **a** The reference (or current) configuration at time t. **b** Position of a closest point pair on the contact interface at time $t + \Delta t$ under the local and global coordinates

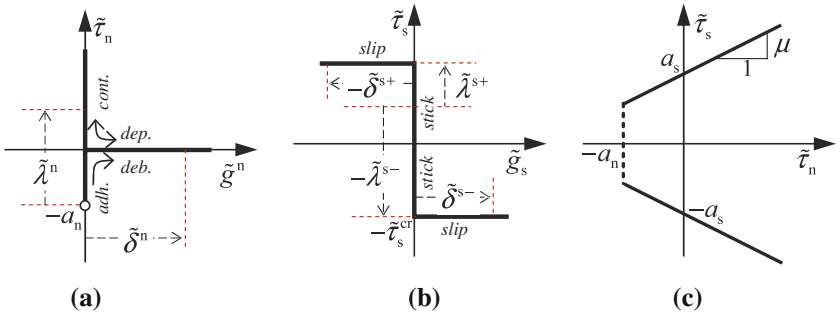

Fig. 3 Contact interface model. **a** Normal contact model. **b** Tangential friction model. **c** Modified Coulomb frictional contact law

illustrates a potential contact interface $\Gamma_{\mathrm{CI}}^{(\beta)}$ is composed of contact surfaces $\Gamma_{\mathrm{c}}^{(\beta_1)}$ and $\Gamma_{\mathrm{c}}^{(\beta_2)}$ from arbitrary two bodies β_1 and β_2, respectively, as shown in Fig. 2. Let points $\boldsymbol{x}^{(\beta_1)}$ and $\boldsymbol{x}^{(\beta_2)}$ on the two contact surfaces $\Gamma_{\mathrm{c}}^{(\beta_1)}$ and $\Gamma_{\mathrm{c}}^{(\beta_2)}$, respectively, are an arbitrary closest point pair under the reference (or current) configuration (at time t); $\boldsymbol{u}^{(\alpha)} = \boldsymbol{u}^{(\alpha)}\left(\boldsymbol{x}^{(\alpha)}\right)$ is the displacement increment in the current interval Δt and $\tilde{\boldsymbol{x}}^{(\alpha)} = \boldsymbol{x}^{(\alpha)} + \boldsymbol{u}^{(\alpha)}$ represents the position of $\boldsymbol{x}^{(\alpha)}$ $(\alpha = \beta_1, \beta_2)$ at time $t + \Delta t$ under the global coordinate. The behavior of the contact interface can be characterized by the contact traction and gap of the closest point pair under the local coordinate as follows.

3.1.1 Normal contact model

From Fig. 2b, the normal gap $\tilde{g}_{\mathrm{n}}$can be given as

$$\begin{aligned}\tilde{g}_{\mathrm{n}} &= \left(\tilde{\boldsymbol{x}}^{(\beta_2)} - \tilde{\boldsymbol{x}}^{(\beta_1)}\right)\boldsymbol{n} \\ &= \left[\left(\boldsymbol{x}^{(\beta_2)} - \boldsymbol{x}^{(\beta_1)}\right) + \left(\boldsymbol{u}^{(\beta_2)} - \boldsymbol{u}^{(\beta_1)}\right)\right]^{\mathrm{T}}\boldsymbol{n} \\ &= \left(\boldsymbol{g}_t + \boldsymbol{g}\right)^{\mathrm{T}}\boldsymbol{n} \end{aligned} \tag{3.1}$$

where $\boldsymbol{g}_t = \boldsymbol{x}^{(\beta_2)} - \boldsymbol{x}^{(\beta_1)}$ and $\boldsymbol{g} = \boldsymbol{u}^{(\beta_2)} - \boldsymbol{u}^{(\beta_1)}$ are, respectively, current initial and incremental gaps under the global coordinate, and $\boldsymbol{n} = \left[n_x\ n_y\right]^{\mathrm{T}}$ represents the outward normal vector as shown in Fig. 2.

Considering the normal adhesion, the normal contact model that governs the relation between the normal contact traction $\tilde{\tau}_{\mathrm{n}}$ and gap $\tilde{g}_{\mathrm{n}}$ as shown in Fig. 3a can be represented as an equality condition of complementarity [57]:

$$\tilde{\tau}_{\mathrm{n}}\tilde{g}_{\mathrm{n}} = 0, \quad \tilde{\tau}_{\mathrm{n}} \geq -a_{\mathrm{n}}, \quad \tilde{g}_{\mathrm{n}} \geq 0 \tag{3.2}$$

where a_{n} is a threshold of normal adhesion for tension, and the pressure is positive here.

It can be divided into four states as shown in Fig. 3a:

$$\begin{cases} 0 > \tilde{\tau}_{\mathrm{n}} > -a_{\mathrm{n}} (\tilde{g}_{\mathrm{n}} = 0) & \text{normal adhesion} \\ \tilde{\tau}_{\mathrm{n}} = 0\ (\tilde{g}_{\mathrm{n}} > 0) & \text{debonding } (a_{\mathrm{n}} > 0) \\ & \text{or departing } (a_{\mathrm{n}} = 0) \\ \tilde{\tau}_{\mathrm{n}} > 0 (\tilde{g}_{\mathrm{n}} = 0) & \text{contacting} \end{cases} \tag{3.3}$$

Note that this unilateral adhesive contact graph is not monotone function and has a cusp at $(0, -a_{\mathrm{n}})$ [57]. In addition, normal adhesion is an irreversible phenomenon called debonding as shown in Fig. 3a [57]. In the absence of normal adhesion $(a_{\mathrm{n}} = 0)$, the contact model can be degraded to the classical unilateral contact.

3.1.2 Tangential friction model

Similarly, the tangential slip gap $\tilde{g}_s$ can finally be given as

$$\tilde{g}_s = \left(\boldsymbol{g}_t + \boldsymbol{g}\right)^T \boldsymbol{s} \tag{3.4}$$

where $\boldsymbol{s} = \left[-n_y n_x\right]^T$ is the tangential vector in the right-hand rule as shown in Fig. 2b.

The friction model that governs the general relation between tangential contact traction $\tilde{\tau}_s$ and slip gap $\tilde{g}_s$ can also be given as an equality condition of complementarity (see, Fig. 3b)

$$\left(|\tilde{\tau}_s| - \tau_s^{cr}\right)|\tilde{g}_s| = 0, \quad |\tilde{\tau}_s| \le \tau_s^{cr}, \quad |\tilde{g}_s| \ge 0 \tag{3.5}$$

where τ_s^{cr} is a threshold of tangential contact traction for tangential slip. If the friction model is characterized by Tresca friction [13], we have $\tau_s^{cr} = a_s$, where a_s is a threshold of the tangential adhesion for slipping. For Coulomb friction [13], $\tau_s^{cr} = \mu\tilde{\tau}_n$ and μ is the frictional coefficient. Furthermore, for Coulomb friction with tangential adhesion [58], $\tau_s^{cr} = a_s + \mu\tilde{\tau}_n$.

The Eq. (3.5) can be decomposed into two states:

$$\begin{cases} |\tilde{\tau}_s| < \tau_s^{cr} \ (g_s = 0) & \text{sticking} \\ \tilde{\tau}_s = \pm\tau_s^{cr} \ (g_s \ne 0) & \text{slipping} \end{cases} \tag{3.6}$$

3.1.3 Modified Coulomb frictional contact model

In comparison with material plasticity, the normal contact and tangential friction models of the contact are very much similar to the rigid perfectly-plastic constitutive model of material and can be coupled together. The conformability of the contact can be given as follows:

$$\boldsymbol{f}_c\left(\tilde{\boldsymbol{\tau}}\right) = \left[-\tilde{\tau}_n - a_n, |\tilde{\tau}_s| - a_s - \mu\tilde{\tau}_n\right]^T \le 0 \tag{3.7}$$

$$\boldsymbol{f}_g\left(\tilde{\boldsymbol{g}}\right) = \left[\tilde{g}_n, |\tilde{g}_s|\right]^T \ge 0 \tag{3.8}$$

$$\boldsymbol{f}_c^T\left(\tilde{\boldsymbol{\tau}}\right)\boldsymbol{f}_g\left(\tilde{\boldsymbol{g}}\right) = 0 \tag{3.9}$$

where the notation $\boldsymbol{f}_c\left(\tilde{\boldsymbol{\tau}}\right)$ and $\boldsymbol{f}_g\left(\tilde{\boldsymbol{g}}\right)$, respectively, represent "contact yield function" and "gap function". The Eq. (3.7) is a contact yield criterion (modified Coulomb frictional contact law), which considers the normal and tangential adhesions in the forms of constant for simplicity, as shown in Fig. 3c. Note that in the absence of normal and tangential adhesions ($\boldsymbol{a} = 0$), this frictional contact model can be degenerated into the classical Coulomb friction model. The gap function in Eq. (3.8) includes normal and tangential gaps given out in Eqs. (3.2) and (3.5), respectively. The Eq. (3.9) represents the complementarity condition between the contact yield and gap functions.

Clearly, this contact model can represent all contact behaviors. It physically means that when the contact traction does not satisfy the contact yield criterion, the gap is zero. In other words, the two bodies are contacting or bonding together at the normal direction, or sticking together at the tangential direction as shown in Fig. 3a and b. When the contact traction satisfies the contact yield criterion, the gap is larger than zero, or more specifically the two bodies are departing or debonding at the normal direction, or slipping at the tangential direction as shown in Fig. 3a and b.

For the convenience of computation, upon linearization the Eqs. (3.7,3.8,3.9) can be given in the form of matrices:

$$-\tilde{\boldsymbol{M}}_c\tilde{\boldsymbol{\tau}} - \tilde{\boldsymbol{k}} + \tilde{\boldsymbol{\lambda}} = \boldsymbol{0} \tag{3.10}$$

$$\tilde{\boldsymbol{M}}_g\tilde{\boldsymbol{\delta}} - \tilde{\boldsymbol{\Theta}}\tilde{\boldsymbol{g}} = \boldsymbol{0} \tag{3.11}$$

$$\tilde{\boldsymbol{\lambda}}^T\tilde{\boldsymbol{\delta}} = 0, \quad \tilde{\boldsymbol{\lambda}} \ge \boldsymbol{0}, \quad \tilde{\boldsymbol{\delta}} \ge \boldsymbol{0} \tag{3.12}$$

where $\tilde{\boldsymbol{M}}_c = \begin{bmatrix} 1 & \mu & \mu \\ 0 & -1 & 1 \end{bmatrix}^T$, $\tilde{\boldsymbol{M}}_g = \begin{bmatrix} 1 & 0 & 0 \\ 0 & -1 & 1 \end{bmatrix}$, $\tilde{\boldsymbol{k}} = \tilde{\boldsymbol{k}}(\boldsymbol{a}) = [a_n, a_s, a_s]^T$; $\tilde{\boldsymbol{\Theta}} = \tilde{\boldsymbol{\Theta}}(\boldsymbol{n}) = \begin{bmatrix} n_x & n_y \\ -n_y & n_x \end{bmatrix}$ is a rotation matrix from global to local coordinates as shown in Fig. 2b, $\tilde{\boldsymbol{\lambda}} = \left[\tilde{\lambda}^n \ \tilde{\lambda}^{s+} \ \tilde{\lambda}^{s-}\right]^T$ is a vector of slack variables [59] denoting residual strengths in the normal, positive and negative tangential directions as shown in Fig. 3a and b. Correspondingly, $\tilde{\boldsymbol{\delta}} = \left[\tilde{\delta}^n \ \tilde{\delta}^{s+} \ \tilde{\delta}^{s-}\right]^T$ represents gaps at the normal, positive and negative tangential directions (see Fig. 3a and b).

3.2 Discretized form

Once each body is discretized in a solid system using field nodes as discussed in Sect. 2, along all discretized surfaces the contact tractions and deformations must satisfy the conditions of contact compatibility and equilibrium of the system in accordance with the current contact conditions. For convenience, consider a typically discretized contact interface $\Gamma_{CI}^{(\beta)}$ with two equal-length contact surfaces from two rectangular bodies β_1 and β_2 as shown in Fig. 4. For the matching discretization (see Fig. 4a), contact constraints can be enforced by node-to-node contact as in finite element method (FEM). For the non-matching discretization (see Fig. 4b), and assuming that all projected points on the opposite surface of non-matching nodes along the finer surface (assigned surface $\Gamma_c^{(\beta_2)}$ here) are known, the contact constraints can also be enforced by node-to-projected point contact. Therefore, the discretized contact interface can be represented with contact point-pairs (including pairs of node-to-node and node-to-projected point), and each contact point-pair must satisfy the constraints given in Eqs. (3.10,3.11,3.12).

For any contact point-pair k on the contact interface $\Gamma_{CI}^{(\beta)}$ as shown in Fig. 4, utilizing the displacement interpolation the gap increment $\boldsymbol{g}_k$ can be given generally as:

$$\begin{aligned} \boldsymbol{g}_k &= \boldsymbol{u}_k^{(\beta_2)} - \boldsymbol{u}_k^{(\beta_1)} \\ &= \left[-\boldsymbol{N}_k^{(\beta_1)} \boldsymbol{N}_k^{(\beta_2)}\right]\left[\boldsymbol{U}_{sk}^{(\beta_1)} \boldsymbol{U}_{sk}^{(\beta_2)}\right]^T \\ &= \overleftrightarrow{\boldsymbol{N}}_k^{(\beta)} \overleftrightarrow{\boldsymbol{U}}_k^{(\beta)} \end{aligned} \tag{3.13}$$

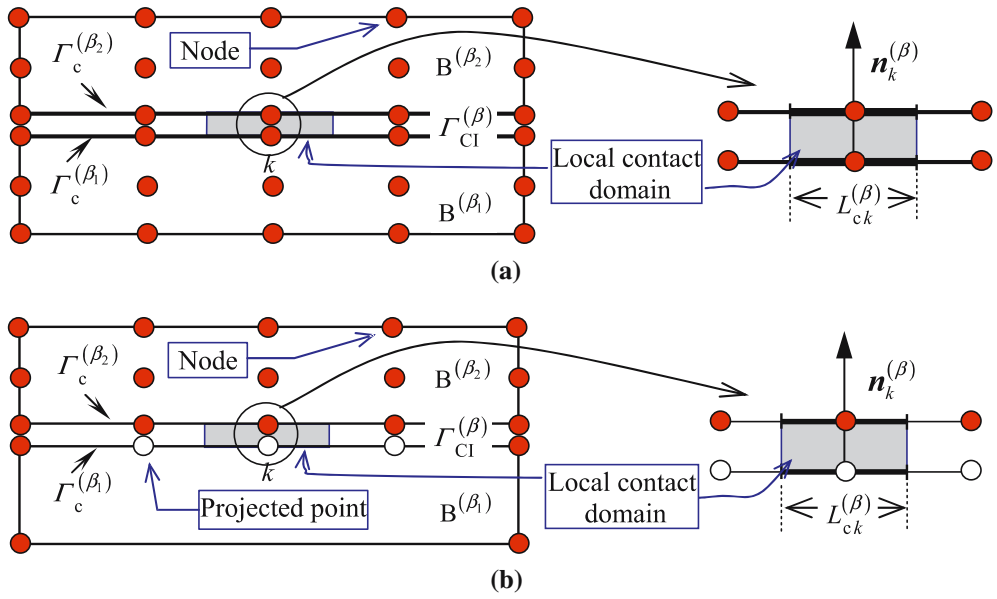

Fig. 4 Typically discretized contact interface and point-to-point contact model. **a** Matching discretization and node-to-node contact model. **b** Non-matching discretization and node-to-Projected point contact model

where $\overleftrightarrow{\boldsymbol{N}}_k^{(\beta)} = \left[-\boldsymbol{N}_k^{(\beta_1)}\boldsymbol{N}_k^{(\beta_2)}\right]$ and $\overleftrightarrow{\boldsymbol{U}}_k^{(\beta)} = \left[\boldsymbol{U}_{sk}^{(\beta_1)}\boldsymbol{U}_{sk}^{(\beta_2)}\right]^{\mathrm{T}}$, $\boldsymbol{N}_k^{(\beta_n)}$ and $\boldsymbol{U}_{sk}^{(\beta_n)}$ are, respectively, interpolation shape functions and generalized displacement increment of the kth contact point (node or projected point) on the contact surface of body β_n ($n = 1, 2$).

Considering $\tilde{\boldsymbol{\tau}}_k^{(\beta)} = \boldsymbol{\tau}_{tk}^{(\beta)} + \boldsymbol{\tau}_k^{(\beta)}$, $\boldsymbol{\tau}_{tk}^{(\beta)}$ and $\boldsymbol{\tau}_k^{(\beta)}$ are the initial and incremental contact tractions of the kth contact point-pair. It has to satisfy the following equations in incremental form:

$$-\boldsymbol{M}_{ck}^{(\beta)}\boldsymbol{\tau}_k^{(\beta)} + \boldsymbol{\lambda}_k^{(\beta)} = \boldsymbol{k}_k^{(\beta)} + \boldsymbol{M}_{ck}^{(\beta)}\boldsymbol{\tau}_{tk}^{(\beta)} \tag{3.14}$$

$$\boldsymbol{M}_{gk}^{(\beta)}\boldsymbol{\delta}_k^{(\beta)} - \boldsymbol{G}_k^{(\beta)}\overleftrightarrow{\boldsymbol{U}}_k^{(\beta)} = \boldsymbol{G}_{tk}^{(\beta)} \tag{3.15}$$

$$\boldsymbol{\lambda}_k^{(\beta)\mathrm{T}}\boldsymbol{\delta}_k^{(\beta)} = 0, \quad \boldsymbol{\lambda}_k^{(\beta)} \geq \boldsymbol{0}; \quad \boldsymbol{\delta}_k^{(\beta)} \geq \boldsymbol{0} \tag{3.16}$$

where $\boldsymbol{M}_{ck}^{(\beta)} = \tilde{\boldsymbol{M}}_c(\mu_\beta)$, $\boldsymbol{M}_{gk}^{(\beta)} = \tilde{\boldsymbol{M}}_g$, $\boldsymbol{k}_k^{(\beta)} = \tilde{\boldsymbol{k}}(\mathbf{a}_\beta)$, $\boldsymbol{\Theta}_k^{(\beta)} = \tilde{\boldsymbol{\Theta}}\left(\boldsymbol{n}_k^{(\beta)}\right)$, $\boldsymbol{G}_k^{(\beta)} = \boldsymbol{\Theta}_k^{(\beta)}\overleftrightarrow{\boldsymbol{N}}_k^{(\beta)}$, $\boldsymbol{\lambda}_k^{(\beta)} = \left[\lambda_k^{(\beta)\mathrm{n}}\lambda_k^{(\beta)\mathrm{s}+}\lambda_k^{(\beta)\mathrm{s}-}\right]^{\mathrm{T}}$ and $\boldsymbol{\delta}_k^{(\beta)} = \left[\delta_k^{(\beta)\mathrm{n}+}\delta_k^{(\beta)\mathrm{s}+}\delta_k^{(\beta)\mathrm{s}-}\right]^{\mathrm{T}}$. $\boldsymbol{G}_{tk}^{(\beta)} = \boldsymbol{\Theta}_{tk}^{(\beta)}\boldsymbol{g}_{tk}^{(\beta)}$ is the current initial gap for the kth contact point-pair under the local coordinate, $\boldsymbol{a}_\beta$ and μ_β are the adhesion and frictional coefficient of the contact interface $\Gamma_{\mathrm{CI}}^{(\beta)}$.

Assembling all contact contact-pairs on the contact interface $\Gamma_{\mathrm{CI}}^{(\beta)}$, we have

$$-\boldsymbol{M}_c^{(\beta)}\boldsymbol{\tau}^{(\beta)} + \boldsymbol{\lambda}^{(\beta)} = \boldsymbol{k}^{(\beta)} + \boldsymbol{M}_c^{(\beta)}\boldsymbol{\tau}_t^{(\beta)} \tag{3.17}$$

$$\boldsymbol{M}_g^{(\beta)}\boldsymbol{\delta}^{(\beta)} - \boldsymbol{G}^{(\beta)}\overleftrightarrow{\boldsymbol{U}}^{(\beta)} = \boldsymbol{G}_t^{(\beta)} \tag{3.18}$$

$$\boldsymbol{\lambda}^{(\beta)\mathrm{T}}\boldsymbol{\delta}^{(\beta)} = 0\left(\boldsymbol{\lambda}^{(\beta)} \geq 0; \boldsymbol{\delta}^{(\beta)} \geq 0\right) \tag{3.19}$$

where $\boldsymbol{M}_c^{(\beta)} = \mathrm{diag}\left[\boldsymbol{M}_{ck}^{(\beta)}\right]$ and $\boldsymbol{M}_g^{(\beta)} = \mathrm{diag}\left[\boldsymbol{M}_{gk}^{(\beta)}\right](k = 1, 2, \ldots, n_{\mathrm{cp}}^{(\beta)})$; $\boldsymbol{G}^{(\beta)} = \left[\boldsymbol{G}_1^{(\beta)}, \boldsymbol{G}_2^{(\beta)}, \ldots, \boldsymbol{G}_{n_{\mathrm{cp}}^{(\beta)}}^{(\beta)}\right]^{\mathrm{T}}$, $\overleftrightarrow{\boldsymbol{U}}^{(\beta)} = \cup\overleftrightarrow{\boldsymbol{U}}_k^{(\beta)}\left(k = 1, 2, \ldots, n_{\mathrm{cp}}^{(\beta)}\right)$. $\boldsymbol{G}_t^{(\beta)}$, $\boldsymbol{\tau}_t^{(\beta)}$, $\boldsymbol{k}^{(\beta)}$, $\boldsymbol{\lambda}^{(\beta)}$ and $\boldsymbol{\delta}^{(\beta)}$ are, respectively, vectors collecting all $\boldsymbol{G}_{tk}^{(\beta)}$, $\boldsymbol{\tau}_{tk}^{(\beta)}$, $\boldsymbol{k}_k^{(\beta)}$, $\boldsymbol{\lambda}_k^{(\beta)}$ and $\boldsymbol{\delta}_k^{(\beta)}(k = 1, 2, \ldots, n_{\mathrm{cp}}^{(\beta)})$, and $n_{\mathrm{cp}}^{(\beta)}$ is the number of contact point-pairs on the contact interface $\Gamma_{\mathrm{CI}}^{(\beta)}$.

Note that, for the contact interface $\Gamma_{\mathrm{CI}}^{(\beta)}$, the Eqs. (3.17, 3.18, 3.19), respectively, represent the discretized forms of the contact yield criterion (modified Coulomb frictional contact law), gap, and equality condition of complementarity.

The functional increment $\Pi_c^{(\beta)}$ of the contribution of the contact interface $\Gamma_{\mathrm{CI}}^{(\beta)}$ can be given as

$$\Pi_c^{(\beta)} = \int_{\Gamma_{\mathrm{CI}}^{(\beta)}} (\boldsymbol{\Theta}\boldsymbol{g})^{\mathrm{T}}\boldsymbol{\tau}\,\mathrm{d}\Gamma \tag{3.20}$$

Using the trapezoidal integration and displacement interpolation, $\Pi_c^{(\beta)}$ can be written in discrete form:

$$\begin{aligned}\Pi_c^{(\beta)} &= \sum_{k=1}^{n_{cp}^{(\beta)}} \overleftrightarrow{\boldsymbol{U}}_k^{(\beta)\mathrm{T}}\boldsymbol{G}_k^{(\beta)\mathrm{T}}\boldsymbol{\tau}_k^{(\beta)}L_{ck}^{(\beta)} \\ &= \overleftrightarrow{\boldsymbol{U}}^{(\beta)\mathrm{T}}\boldsymbol{G}^{(\beta)\mathrm{T}}\boldsymbol{L}_c^{(\beta)}\boldsymbol{\tau}^{(\beta)}\end{aligned} \tag{3.21}$$

where $\boldsymbol{L}_c^{(\beta)} = \mathrm{diag}\left[L_{ck}^{(\beta)}\boldsymbol{I}_2\right](k = 1, 2, \ldots, n_{ij}^{\mathrm{cp}})$, $L_{ck}^{(\beta)}$ is the length of the kth contact point-pair on the contact interface $\Gamma_{\mathrm{CI}}^{(\beta)}$ as shown in Fig. 4, and $\boldsymbol{I}_2$ is a unit matrix of 2×2.

4 Subdomain parametric variational principle and discretization

4.1 Weak form of equations for frictional contact

Consider a solid system consisting of n_B bodies. At time t the configuration of the entire system Ω (domain) is known, and $\Omega^{(i)}$ (subdomain) represents the configuration of the ith body bounded by $\Gamma\left(\Omega^{(i)}\right) = \Gamma_u^{(i)} \cup \Gamma_t^{(i)} \cup \Gamma_c^{(i)}$, in which $\Gamma_u^{(i)}$, $\Gamma_t^{(i)}$ and $\Gamma_c^{(i)}$ are, respectively, the displacement, traction and contact boundaries of body i. For body i, the incremental form of its boundary value equation may be described in the standard form as follows:

(1) The static equilibrium equation is given as

$$\boldsymbol{B}^{\mathrm{T}}\boldsymbol{\sigma}^{(i)} + \boldsymbol{b}^{(i)} = 0 \quad \text{in } \Omega^{(i)} \tag{4.1}$$

where $\boldsymbol{\sigma}^{(i)} = \left[\sigma_{xx}^{(i)}, \sigma_{yy}^{(i)}, \tau_{xy}^{(i)}\right]^{\mathrm{T}}$ and $\boldsymbol{b}^{(i)}$ are, respectively, vectors of the stress increment and body force density increment for body i.

(2) The geometric continuity equation (or strain–displacement relation) is given as

$$\boldsymbol{\varepsilon}^{(i)} = \boldsymbol{B}\boldsymbol{u}^{(i)} \tag{4.2}$$

where $\boldsymbol{\varepsilon}^{(i)} = \left[\varepsilon_{xx}^{(i)}, \varepsilon_{yy}^{(i)}, \gamma_{xy}^{(i)}\right]^{\mathrm{T}}$ and $\boldsymbol{u}^{(i)} = \left[u^{(i)}, v^{(i)}\right]^{\mathrm{T}}$ are vectors of strain increment and displacement increment.

(3) The constitutional equation is given as

$$\boldsymbol{\sigma}^{(i)} = \boldsymbol{D}^{(i)}\boldsymbol{\varepsilon}^{(i)} \tag{4.3}$$

where $\boldsymbol{D}^{(i)}$ is a matrix of elastic constants of the material. For plane stress problems it is represented with Young's modulus E_i and Poisson's ratio ν_i as

$$\boldsymbol{D}^{(i)} = \frac{E_i}{1-\nu_i^2}\begin{bmatrix} 1 & \nu_i & 0 \\ \nu_i & 1 & 0 \\ 0 & 0 & \frac{1-\nu_i}{2} \end{bmatrix} \tag{4.4}$$

For plane strain problems, the above holds after replacing E_i and ν_i with $E_i/\left(1-\nu_i^2\right)$ and $\nu_i/(1-\nu_i)$, respectively.

(4) The boundary conditions

The displacement boundary condition can be given as

$$\boldsymbol{u}^{(i)} = \bar{\boldsymbol{u}}^{(i)} \quad \text{on } \Gamma_u^{(i)} \tag{4.5}$$

where $\bar{\boldsymbol{u}}^{(i)}$ is a given displacement increment at boundary $\Gamma_u^{(i)}$.

The traction boundary condition is given as

$$\boldsymbol{t}^{(i)} = \tilde{\boldsymbol{n}}\boldsymbol{\sigma}^{(i)} = \bar{\boldsymbol{t}}^{(i)} \quad \text{on } \Gamma_t^{(i)} \tag{4.6}$$

where $\bar{\boldsymbol{t}}^{(i)}$ is a given traction increment at boundary $\Gamma_t^{(i)}$, and $\tilde{\boldsymbol{n}} = \begin{bmatrix} n_x^{(i)} & 0 & n_y^{(i)} \\ 0 & n_y^{(i)} & n_x^{(i)} \end{bmatrix}$.

The contact boundary condition is given as

$$\boldsymbol{\Theta}^{(i)\mathrm{T}}\boldsymbol{\tau}^{(i)} = \tilde{\boldsymbol{n}}\boldsymbol{\sigma}^{(i)} \quad \text{on } \Gamma_c^{(i)} \tag{4.7}$$

where $\boldsymbol{\tau}^{(i)}$ is the contact traction increment on the contact boundary $\Gamma_c^{(i)}$ under the constraints of frictional contact as given in Eqs. (3.10,3.11,3.12).

4.2 Subdomain parametric variational principle (SPVP)

By applying virtual displacement increment $\delta\boldsymbol{u}^{(i)}$ to the ith body under the current configuration, the increment of virtual potential energy $\delta\Pi_e^{(i)}$ and virtual work increment done by external incremental force (including incremental contact traction) $\delta W_{\mathrm{ext}}^{(i)}\left(\boldsymbol{\tau}^{(i)}\right)$ are, respectively, given as

$$\begin{aligned}\delta\Pi_e^{(i)} &= \int_{\Omega^{(i)}} \delta\boldsymbol{\varepsilon}^{(i)\mathrm{T}}\boldsymbol{\sigma}^{(i)}\mathrm{d}\Omega \\ &= \int_{\Gamma^{(i)}} \delta\boldsymbol{u}^{(i)\mathrm{T}}\tilde{\boldsymbol{n}}\boldsymbol{\sigma}^{(i)}\mathrm{d}\Gamma - \int_{\Omega^{(i)}} \delta\boldsymbol{u}^{(i)\mathrm{T}}\boldsymbol{B}^{\mathrm{T}}\boldsymbol{\sigma}^{(i)}\mathrm{d}\Omega\end{aligned} \tag{4.8}$$

$$\begin{aligned}\delta W_{\mathrm{ext}}^{(i)}\left(\boldsymbol{\tau}^{(i)}\right) &= \int_{\Omega^{(i)}} \delta\boldsymbol{u}^{(i)\mathrm{T}}\boldsymbol{b}^{(i)}\mathrm{d}\Omega + \int_{\Gamma_t^{(i)}} \delta\boldsymbol{u}^{(i)\mathrm{T}}\bar{\boldsymbol{t}}^{(i)}\mathrm{d}\Gamma \\ &\quad + \int_{\Gamma_c^{(i)}} \delta\boldsymbol{u}^{(i)\mathrm{T}}\boldsymbol{\Theta}^{(i)\mathrm{T}}\boldsymbol{\tau}^{(i)}\mathrm{d}\Gamma\end{aligned} \tag{4.9}$$

Since the virtual work increment $\delta W_{\mathrm{ext}}^{(i)}\left(\boldsymbol{\tau}^{(i)}\right)$ is equal to the increment of virtual potential energy $\delta\Pi_e^{(i)}$ according to virtual work principle, we have

$$\begin{aligned}&\int_{\Omega^{(i)}} \delta\boldsymbol{u}^{(i)\mathrm{T}}\left(\boldsymbol{B}^{\mathrm{T}}\boldsymbol{\sigma}^{(i)} + \boldsymbol{b}^{(i)}\right)\mathrm{d}\Omega \\ &- \int_{\Gamma_t^{(i)}} \delta\boldsymbol{u}^{(i)\mathrm{T}}\left(\tilde{\boldsymbol{n}}\boldsymbol{\sigma}^{(i)} - \bar{\boldsymbol{t}}^{(i)}\right)\mathrm{d}\Gamma \\ &- \int_{\Gamma_c^{(i)}} \delta\boldsymbol{u}^{(i)\mathrm{T}}\left(\tilde{\boldsymbol{n}}\boldsymbol{\sigma}^{(i)} - \boldsymbol{\Theta}^{(i)\mathrm{T}}\boldsymbol{\tau}^{(i)}\right)\mathrm{d}\Gamma = 0\end{aligned} \tag{4.10}$$

From the above equation it is evident that Eqs. (4.1), (4.6) and (4.7) can be derived because that virtual displacement increment $\delta\boldsymbol{u}^{(i)}$ is arbitrary.

Therefore, for body i, the functional of its potential energy increment $\Pi^{(i)}\left(\boldsymbol{\tau}^{(i)}\right)$ can be represented as

$$\begin{aligned}\Pi^{(i)}\left(\boldsymbol{\tau}^{(i)}\right) &= \frac{1}{2}\int_{\Omega^{(i)}} \boldsymbol{\varepsilon}^{(i)\mathrm{T}}\boldsymbol{D}^{(i)}\boldsymbol{\varepsilon}^{(i)}\mathrm{d}\Omega - \int_{\Omega^{(i)}} \boldsymbol{u}^{(i)\mathrm{T}}\boldsymbol{b}^{(i)}\mathrm{d}\Omega \\ &\quad - \int_{\Gamma_t^{(i)}} \boldsymbol{u}^{(i)}\bar{\boldsymbol{t}}^{(i)\mathrm{d}\Gamma} - \int_{\Gamma_c^{(i)}} \boldsymbol{u}^{(i)\mathrm{T}}\boldsymbol{\Theta}^{(i)\mathrm{T}}\boldsymbol{\tau}^{(i)}\mathrm{d}\Gamma\end{aligned} \tag{4.11}$$

The parametric variational form [59, 60] of the potential energy increment for body i can now be derived as

$$\delta\Pi^{(i)}\left(\boldsymbol{\tau}^{(i)}\right) = \int_{\Omega^{(i)}} \delta\boldsymbol{\varepsilon}^{(i)\mathrm{T}}\boldsymbol{D}^{(i)}\boldsymbol{\varepsilon}^{(i)}\mathrm{d}\Omega - \int_{\Omega^{(i)}} \delta\boldsymbol{u}^{(i)\mathrm{T}}\boldsymbol{b}^{(i)}\mathrm{d}\Omega - \int_{\Gamma_{\mathrm{t}}^{(i)}} \delta\boldsymbol{u}^{(i)\mathrm{T}}\bar{\boldsymbol{t}}^{(i)}\mathrm{d}\Gamma - \int_{\Gamma_{\mathrm{c}}^{(i)}} \delta\boldsymbol{u}^{(i)\mathrm{T}}\boldsymbol{\Theta}^{(i)\mathrm{T}}\boldsymbol{\tau}^{(i)}\mathrm{d}\Gamma = 0 \tag{4.12}$$

Note that the contact traction increment $\boldsymbol{\tau}^{(i)}$, which is token as a parametric vector subjected to the constraints given in Eqs. (3.10, 3.11, 3.12), does not take part in the variation. Accordingly the variational principle may be named subdomain parametric variational principle (SPVP).

4.3 Discrete governing equations

The discretized equation can now be obtained using numerical nodal integration of the LC-RPIM, which gives

$$\delta\Pi^{(i)}\left(\boldsymbol{\tau}^{(i)}\right) = \delta\boldsymbol{U}^{(i)\mathrm{T}}\left\{\left(\sum_{j=1}^{n_{\mathrm{n}}^{(i)}}\tilde{\boldsymbol{B}}_j^{(i)\mathrm{T}}\boldsymbol{D}^{(i)}\tilde{\boldsymbol{B}}_j^{(i)}A_j^{(i)}\right)\boldsymbol{U}^{(i)} - \left(\sum_{j=1}^{n_{\mathrm{n}}^{(i)}}\boldsymbol{N}_j^{(i)\mathrm{T}}\boldsymbol{b}^{(i)}A_j^{(i)} + \sum_{j=1}^{n_{\mathrm{t}}^{(i)}}\boldsymbol{N}_j^{(i)\mathrm{T}}\bar{\boldsymbol{t}}_j^{(i)}L_j^{(i)} + \sum_{j=1}^{n_{\mathrm{bcp}}^{(i)}}\boldsymbol{N}_j^{(i)\mathrm{T}}\boldsymbol{\Theta}_j^{(i)\mathrm{T}}\boldsymbol{\tau}_j^{(i)}L_{cj}^{(i)}\right)\right\} = 0 \tag{4.13}$$

where $\boldsymbol{U}^{(i)} = \left[u_1^{(i)}, v_1^{(i)}, u_2^{(i)}, v_2^{(i)}, \ldots, u_{n_{\mathrm{n}}^{(i)}}^{(i)}, v_{n_{\mathrm{n}}^{(i)}}^{(i)}\right]^{\mathrm{T}}$. For the ith body, $n_{\mathrm{n}}^{(i)}$ is the number of its all field nodes, $n_{\mathrm{t}}^{(i)}$ represents the numbers of nodes on its traction boundary, and $n_{\mathrm{bcp}}^{(i)}$ is the number of contact point-pairs on its contact boundary. $A_j^{(i)}$ and $L_j^{(i)}$ are, respectively, area and boundary length possessed by node $\boldsymbol{x}_j^{(i)}$ (the jth nodes in body i), and

$$\boldsymbol{N}_j^{(i)} = \boldsymbol{N}\left(\boldsymbol{x}_j^{(i)}\right) = \left[\boldsymbol{N}_1^{(ij)}, \boldsymbol{N}_2^{(ij)}, \ldots, \boldsymbol{N}_k^{(ij)}, \ldots \boldsymbol{N}_{n_{\mathrm{d}}^{(ij)}}^{(ij)}\right] \tag{4.14}$$

$$\tilde{\boldsymbol{B}}_j^{(i)} = \tilde{\boldsymbol{B}}\left(\boldsymbol{x}_j^{(i)}\right) = \left[\tilde{\boldsymbol{B}}_1^{(ij)}, \tilde{\boldsymbol{B}}_2^{(ij)}, \ldots, \tilde{\boldsymbol{B}}_k^{(ij)} \ldots, \tilde{\boldsymbol{B}}_{n_{\mathrm{g}}^{(ij)}}^{(ij)}\right] \tag{4.15}$$

where $\boldsymbol{N}_k^{(ij)} = \begin{bmatrix} N_k^{(ij)} & 0 \\ 0 & N_k^{(ij)} \end{bmatrix}$ and $N_k^{(ij)} = N_k\left(\boldsymbol{x}_j^{(i)}\right)$ computed by Eq. (2.3), $\tilde{B}_k^{(ij)} = \begin{bmatrix} \bar{B}_{xk}^{(ij)} & 0 & \bar{B}_{yk}^{(ij)} \\ 0 & \bar{B}_{yk}^{(ij)} & \bar{B}_{xk}^{(ij)} \end{bmatrix}^{\mathrm{T}}$ and $\bar{\boldsymbol{B}}_k^{(ij)} = \bar{\boldsymbol{B}}_k\left(\boldsymbol{x}_j^{(i)}\right) = \left[\bar{B}_{kx}^{(ij)}\ \bar{B}_{ky}^{(ij)}\right]^{\mathrm{T}}$ obtained by Eq. (2.11). $n_{\mathrm{d}}^{(ij)}$ and $n_{\mathrm{g}}^{(ij)}$, respectively, represent the numbers of field nodes used in creating the LC-RPIM shape functions and gradient smoothing for node $\boldsymbol{x}_j^{(i)}$.

Invoking $\delta\Pi^{(i)}\left(\boldsymbol{\tau}^{(i)}\right) = 0$ for any $\delta\boldsymbol{U}^{(i)}$, we can obtain a set of linear algebraic equations

$$\left(\sum_{j=1}^{n_{\mathrm{n}}^{(i)}}\tilde{\boldsymbol{B}}_j^{(i)\mathrm{T}}\boldsymbol{D}^{(i)}\tilde{\boldsymbol{B}}_j^{(i)}A_j^{(i)}\right)\boldsymbol{U}^{(i)} = \sum_{j=1}^{n_{\mathrm{n}}^{(i)}}\boldsymbol{N}_j^{(i)\mathrm{T}}\boldsymbol{b}^{(i)}A_j^{(i)} + \sum_{j=1}^{n_t^{(i)}}\boldsymbol{N}_j^{(i)\mathrm{T}}\bar{\boldsymbol{t}}_j^{(i)}L_j^{(i)} + \sum_{j=1}^{n_{\mathrm{bcp}}^{(i)}}\boldsymbol{N}_j^{(i)\mathrm{T}}\boldsymbol{\Theta}_j^{(i)\mathrm{T}}\boldsymbol{\tau}_j^{(i)}L_{\mathrm{c}j}^{(i)} \tag{4.16}$$

or in matrix form

$$\boldsymbol{K}^{(i)}\boldsymbol{U}^{(i)} - \boldsymbol{C}^{(i)}\boldsymbol{\tau}^{(i)} = \boldsymbol{F}^{(i)} \tag{4.17}$$

in which

$$\boldsymbol{K}^{(i)} = \sum_{j=1}^{n_{\mathrm{n}}^{(i)}}\boldsymbol{K}_{\mathrm{e}j}^{(i)} \tag{4.18}$$

$$\boldsymbol{F}^{(i)} = \sum_{j=1}^{n_{\mathrm{n}}^{(i)}}\boldsymbol{F}_{\mathrm{b}j}^{(i)} + \sum_{j=1}^{n_t^{(i)}}\boldsymbol{F}_{\mathrm{t}j}^{(i)} \tag{4.19}$$

where $\boldsymbol{C}^{(i)} = \left[\boldsymbol{C}_1^{(i)}, \boldsymbol{C}_2^{(i)}, \ldots, \boldsymbol{C}_k^{(i)}, \ldots, \boldsymbol{C}_{n_{\mathrm{bcp}}^{(i)}}^{(i)}\right]$, $\boldsymbol{C}_k^{(i)} = \boldsymbol{N}_j^{(i)\mathrm{T}}\boldsymbol{\Theta}_j^{(i)\mathrm{T}}L_{\mathrm{c}j}^{(i)}$, $\boldsymbol{K}_{\mathrm{e}j}^{(i)} = \tilde{\boldsymbol{B}}_j^{(i)\mathrm{T}}\boldsymbol{D}^{(i)}\tilde{\boldsymbol{B}}_j^{(i)}A_j^{(i)}$, $\boldsymbol{F}_{\mathrm{b}j}^{(i)} = \boldsymbol{N}_j^{(i)}\boldsymbol{b}^{(i)}A_j^{(i)}$ and $\boldsymbol{F}_{\mathrm{t}j}^{(i)} = \boldsymbol{N}_j^{(i)\mathrm{T}}\bar{\boldsymbol{t}}_j^{(i)}L_j^{(i)}$.

Note that the elastic stiffness matrix $\boldsymbol{K}^{(i)}$ may be singular if body i is a suspended solid (namely without displacement boundaries or constraints for rigid body movement) for static analysis. To avoid such singularity, the stiffness matrix $\boldsymbol{K}^{(i)}$ in Eq. (4.18) may be modified as follows:

$$\boldsymbol{K}^{(i)} = \sum_{j=1}^{n_{\mathrm{n}}^{(i)}}\left(\boldsymbol{K}_{\mathrm{e}j}^{(i)} + \boldsymbol{K}_{\mathrm{sd}j}^{(i)}\right) \tag{4.20}$$

where $\boldsymbol{K}_{\mathrm{sd}j}^{(i)} = \alpha_{\mathrm{sd}}^{(i)}E_iA_j^{(i)}\boldsymbol{N}_j^{(i)\mathrm{T}}\boldsymbol{N}_j^{(i)}$ is a small artificial damping matrix (similar to the mass damping matrix for dynamical analysis) for the jth node in body i that is about $\alpha_{\mathrm{sd}}^{(i)}$ order of its elastic stiffness matrix $\boldsymbol{K}_{\mathrm{e}j}^{(i)}$. $\alpha_{\mathrm{sd}}^{(i)}$ is a given coefficient which may be chosen between $10^{-5} \sim 10^{-10}$ according to our numerical testing.

Now assembling all discretized equations of all bodies and contact interfaces, we obtain

$$\boldsymbol{K}\boldsymbol{U} - \boldsymbol{C}\boldsymbol{\tau} = \boldsymbol{F} \tag{4.21}$$

$$-\boldsymbol{M}_{\mathrm{c}}\boldsymbol{\tau} + \boldsymbol{\lambda} = \boldsymbol{k} + \boldsymbol{M}_{\mathrm{c}}\boldsymbol{\tau}_t \tag{4.22}$$

$$\boldsymbol{M}_{\mathrm{g}}\boldsymbol{\delta} - \boldsymbol{G}\boldsymbol{U} = \boldsymbol{G}_t \tag{4.23}$$

$$\boldsymbol{\lambda}^{\mathrm{T}}\boldsymbol{\delta} = 0, \quad \boldsymbol{\lambda} \geq 0, \quad \boldsymbol{\delta} \geq \mathbf{0} \tag{4.24}$$

where $\boldsymbol{K} = \mathrm{diag}\left[\boldsymbol{K}^{(\mathrm{i})}\right]$ (i = 1, 2, ..., n_{B}); $\boldsymbol{C} = \left[\boldsymbol{C}^{(1)}, \boldsymbol{C}^{(2)}, \ldots, \boldsymbol{C}^{(n_B)}\right]$; $\boldsymbol{F} = \left[\boldsymbol{F}^{(1)}, \boldsymbol{F}^{(2)}, \ldots, \boldsymbol{F}^{(n_B)}\right]^{\mathrm{T}}$; $\boldsymbol{U} = \left[\boldsymbol{U}^{(1)}, \boldsymbol{U}^{(2)}, \ldots, \boldsymbol{U}^{(n_B)}\right]^{\mathrm{T}}$; $\boldsymbol{M}_{\mathrm{c}} = \mathrm{diag}\left[\boldsymbol{M}_{\mathrm{c}}^{(\mathrm{i})}\right]$, $\boldsymbol{M}_{\mathrm{g}} = \mathrm{diag}\left[\boldsymbol{M}_{\mathrm{g}}^{(\mathrm{i})}\right]$, and $\boldsymbol{L}_{\mathrm{c}} = \mathrm{diag}\left[\boldsymbol{L}_{\mathrm{c}}^{(\mathrm{i})}\right]$ (i = 1, 2, ..., $\mathrm{n_{CI}}$); $\boldsymbol{G} = \left[\boldsymbol{G}^{(1)}, \boldsymbol{G}^{(2)}, \ldots, \boldsymbol{G}^{(n_{\mathrm{CI}})}\right]^{\mathrm{T}}$; the column vectors $\boldsymbol{\tau}$, $\boldsymbol{\tau}_t$, $\boldsymbol{k}$, $\boldsymbol{G}_t$, $\boldsymbol{\lambda}$ and $\boldsymbol{\delta}$ are composed of $\boldsymbol{\tau}^{(i)}$, $\boldsymbol{\tau}_t^{(i)}$, $\boldsymbol{k}^{(i)}$, $\boldsymbol{G}_t^{(i)}$, $\boldsymbol{\lambda}^{(i)}$ and $\boldsymbol{\delta}^{(i)}$ ($i = 1, 2, \ldots, n_{\mathrm{CI}}$), respectively. In addition, $\boldsymbol{C} = (\boldsymbol{G})^{\mathrm{T}}\boldsymbol{L}_{\mathrm{c}}$. n_{CI} is the number of all potential contact interfaces.

The Eqs. (4.21,4.22,4.23,4.24) are the global discrete governing equations for a solid system with frictional contact. For the convenience of solving them, a transformational treatment is given out as follows.

Note that the stiffness matrix $\boldsymbol{K}$ is symmetric and positive definite (SPD), and thus we can get

$$\boldsymbol{U} = \boldsymbol{K}^{-1}(\boldsymbol{F} + \boldsymbol{C}\boldsymbol{\tau}) \tag{4.25}$$

Substituting Eq. (4.25) into Eq. (4.23), we may obtain

$$\boldsymbol{\tau} = \bar{\boldsymbol{K}}^{-1}\left(\boldsymbol{M}_{\mathrm{c}}\boldsymbol{\delta} - \boldsymbol{G}\boldsymbol{K}^{-1}\boldsymbol{F} - \boldsymbol{G}_t\right) \tag{4.26}$$

where $\bar{\boldsymbol{K}} = \boldsymbol{G}\boldsymbol{C} = \boldsymbol{G}\boldsymbol{K}^{-1}\boldsymbol{G}^{\mathrm{T}}\boldsymbol{L}_{\mathrm{c}}$ is again a positive definite symmetric matrix and reversible.

Then substituting Eq. (4.26) into Eq. (4.22) and considering the constraints in Eq. (4.24), we have

$$\begin{cases} \boldsymbol{\lambda} = \boldsymbol{M}\boldsymbol{\delta} + \boldsymbol{q} \\ \boldsymbol{\lambda}^{\mathrm{T}}\boldsymbol{\delta} = \mathbf{0}, \quad \boldsymbol{\lambda} \geq \mathbf{0}, \quad \boldsymbol{\delta} \geq \mathbf{0} \end{cases} \tag{4.27}$$

where $\boldsymbol{M} = \boldsymbol{M}_{\mathrm{c}}\bar{\boldsymbol{K}}^{-1}\boldsymbol{M}_{\mathrm{g}}$, $\boldsymbol{q} = \boldsymbol{k} + \boldsymbol{M}_{\mathrm{c}}\boldsymbol{\tau}_t - \boldsymbol{M}_{\mathrm{c}}\bar{\boldsymbol{K}}^{-1}\left(\boldsymbol{G}\boldsymbol{K}^{-1}\boldsymbol{F} + \boldsymbol{G}_t\right)$.

It is obvious that the Eq. (4.27) is a standard linear complementarity problem denoted as LCP($\boldsymbol{q}$, $\boldsymbol{M}$). It can be very readily solved using the conventional LCP algorithm such as Lemke method and Dantzig method [61].

5 Numerical examples

An intensive numerical study is conducted to validate the present method. In these examples, MQ-RBF given in Eq. (2.6) and complete linear polynomial basis functions ($m = 3$) are used to construct RPIM shape functions ensuring linear consistency in the local displacement approximation, and the local gradients at the field nodes are obtained using Eq. (2.11). The body force is ignored. Numerical results obtained by the proposed method are compared with those obtained by ABAQUS. In the ABAQUS, we use implicit solver under the condition of small deformation, four-node isoparametric elements, standard surface-to-surface contact with the options of " *small sliding*" for sliding formulation and " *adjust only overclosed nodes*" for slave node adjustment. The contact property for tangential behavior is defined as " *frictionless formulation*" or " *friction formulation using Lagrange Multiplier*". Comparison is also performed with analytical solution, when it is available.

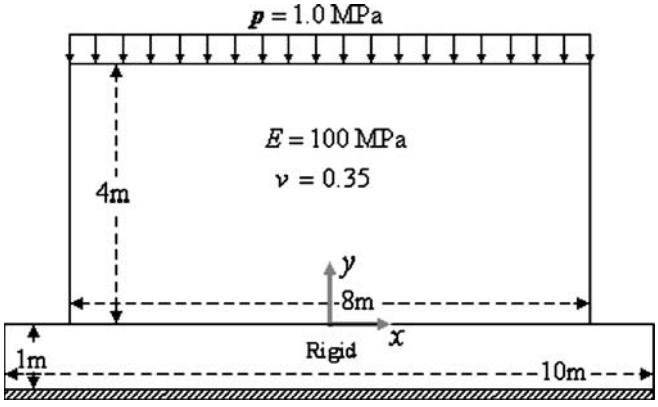

Fig. 5 Contact of an elastic body on a rigid body. The elastic body is subjected to a uniform pressure

5.1 Contact of an elastic body on a rigid body

An elastic body in contact with a rigid body shown in Fig. 5 is firstly studied. The rigid and elastic bodies have the dimensions of $10 \times 1\ \mathrm{m}^2$ and $8 \times 4\ \mathrm{m}^2$, respectively. The elastic body is subjected to a uniform pressure of 1.0 MPa on its top and its material parameters are $E = 10^2$ MPa and $\nu = 0.35$. The plane stress problem is considered. Since this is a symmetrical problem about y axis, only the right half is modeled. In the computation, the rigid body is discretized with four field nodes and the elastic body is discretized with 441 field nodes, and the finite element (FE) mesh for ABAQUS and Voronoi cells with different nodal irregularity for LC-RPIM are shown in Fig. 6.

The irregular nodes are created by altering the coordinates of the regular nodes using the following equations:

$$\begin{cases} x' = x + \Delta x \cdot r_{\mathrm{c}} \cdot \alpha_{\mathrm{ir}} \\ y' = y + \Delta y \cdot r_{\mathrm{c}} \cdot \alpha_{\mathrm{ir}} \end{cases} \tag{5.1}$$

where Δx and Δy are, respectively, the initial regular nodal spacings in the x and y directions; r_{c} is a computer-generated random number between -1.0 to 1.0, and $\alpha_{\mathrm{ir}}$is the irregularity factor.

5.1.1 Effect of the nodal density

In this investigation, the upper elastic body is discretized using three regular nodal patterns including: M1 using 121 of 11×11 field nodes, M2 using 441 of 21×21 field nodes and M3 using 961 of 31×31 field nodes. The dimension of the nodal local support domain $\alpha_{\mathrm{s}} = 2.5$ is used to create RPIM shape functions, and shape parameters used in the MQ-RBF are $\alpha_{\mathrm{c}} = 0.1$ and $q = 1.05$. The contact interface is in the absence of normal and tangential adhesions (in other words, $\boldsymbol{a} = 0$). For frictionless contact ($\mu = 0$), the numerical results of contact pressure and tangential relative slip obtained using the proposed method and ABAQUS are plotted in Fig. 7. It is clearly shown that the results of LC-RPIM agree well with those of ABAQUS. The contact

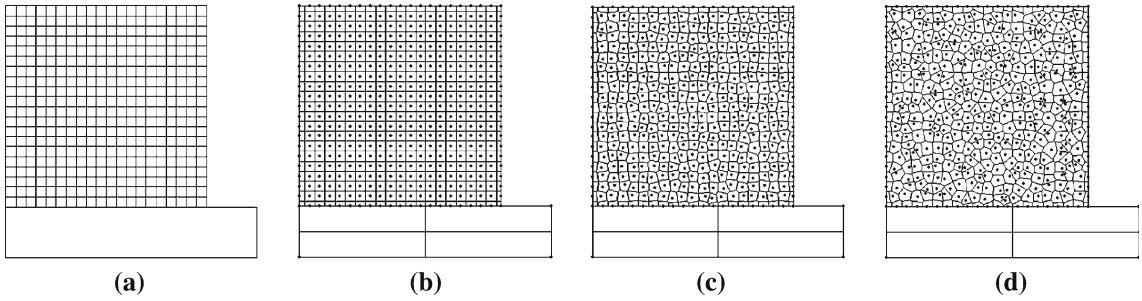

Fig. 6 Nodal distribution and Voronoi cells with different nodal irregularity factors for the contact of an elastic body on a rigid body. **a** FE mesh. **b** Voronoi cells ($\alpha_{ir} = 0.0$). **c** Voronoi cells ($\alpha_{ir} = 0.2$). **d** Voronoi cells ($\alpha_{ir} = 0.4$)

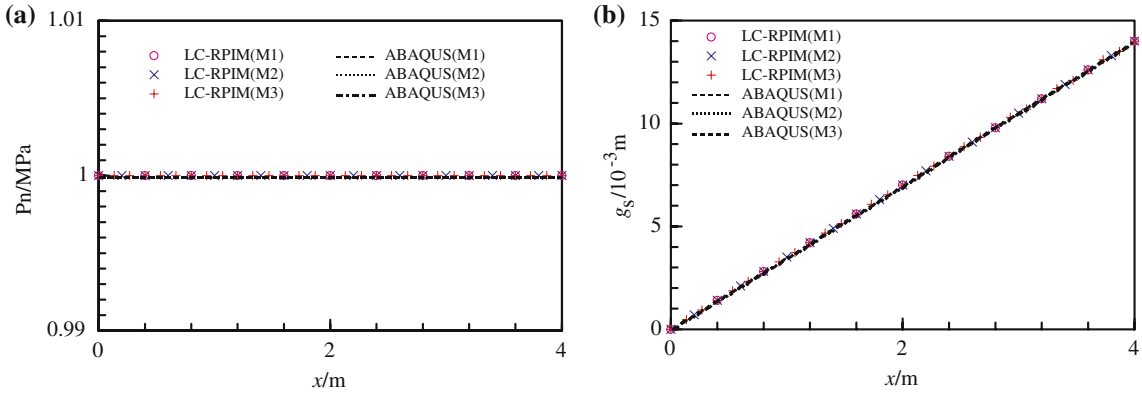

Fig. 7 Effect of nodal density with frictionless contact for the contact of an elastic body on a rigid body ($\alpha_s = 2.5$, $\alpha_c = 0.1$, $q = 1.05$, $\boldsymbol{a} = 0$, $\mu = 0$). **a** Contact pressure. **b** Tangential relative slip

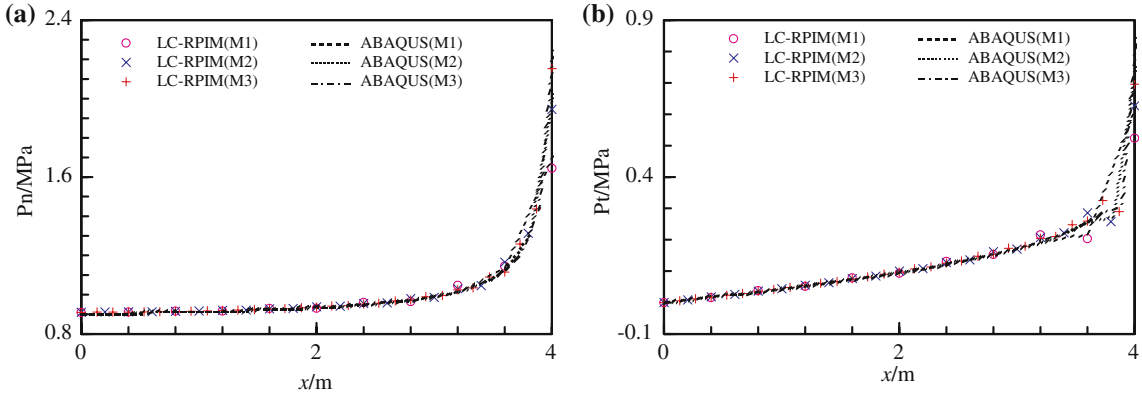

Fig. 8 Effect of nodal density with frictional contact ($\mu = 0.7$) for the contact of an elastic body on a rigid body ($\alpha_s = 2.5$, $\alpha_c = 0.1$, $q = 1.05$, $\boldsymbol{a} = 0$). **a** Contact pressure. **b** Contact shear stress

pressure is uniformly distributed and equal to the applied pressure of 1.0 MPa regardless of the nodal density. Moreover, the tangential relative slip is linear as expected. Next, for frictional contact ($\mu = 0.7$), Fig. 8 illustrates the contact pressure and shear stress computed using the two methods. It is shown that the numerical results of LC-RPIM are in good agreement with those of ABAQUS except slight difference near the right end of the contact interface, where the contact stress concentration occurs and naturally the numerical results depend on the nodal density.

5.1.2 Effect of the tangential adhesion and frictional coefficient

In this study, regularly distributed 441 field nodes are used as shown in Fig. 6a and b, respectively, for ABAQUS and LC-RPIM. Other parameters used are listed in Case C0 row in Table 1. First, numerical results of contact stress and tangential relative slip are plotted in Fig. 9 while varying the tangential adhesion. It is observed that the results of LC-RPIM agree well with those of ABAQUS. With the increase of the

Table 1 Parameters used in different cases

Case	Dimension of nodal support domain α_s	Shape parameters in MQ-RBF		Nodal irregularity factor α_{ir}
		α_c	q	
C0	2.5	0.1	1.05	0.0
C1	1.5	0.1	1.05	0.0
C2	3.5	0.1	1.05	0.0
C3	2.5	0.01	1.05	0.0
C4	2.5	0.1	1.05	0.0
C5	2.5	1.0	0.5	0.0
C6	2.5	0.1	1.5	0.0
C7	2.5	0.1	1.05	0.2
C8	2.5	0.1	1.05	0.4

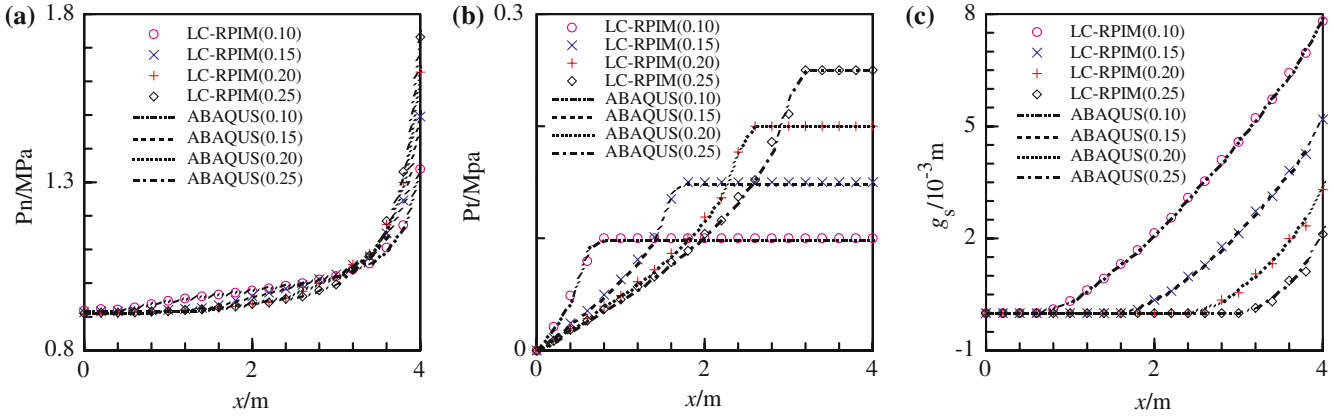

Fig. 9 Effect of the tangential adhesion for the contact of an elastic body on a rigid body ($\alpha_s = 2.5$, $\alpha_c = 0.1$, $q = 1.05$, $a_n = 0$, $\mu = 0$). **a** Contact pressure. **b** Contact shear stress. **c** Tangential relative slip

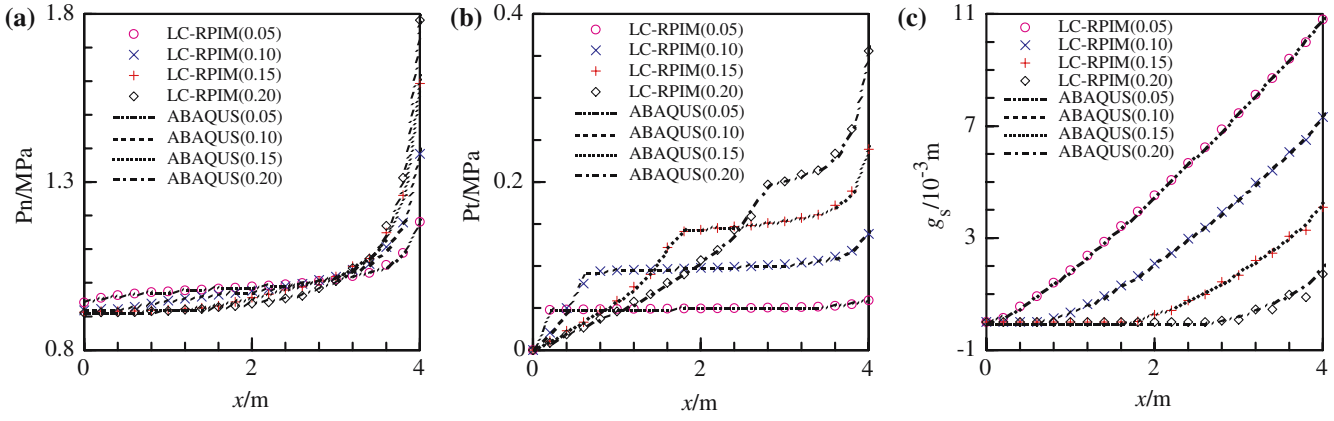

Fig. 10 Effect of the frictional coefficient for the contact of an elastic Body on a rigid body ($\alpha_s = 2.5$, $\alpha_c = 0.1$, $q = 1.05$, $\boldsymbol{a} = 0$). **a** Contact pressure. **b** Contact shear stress. **c** Tangential relative slip

tangential adhesion from 0.1 MPa to 0.25 MPa, contact stress concentration gets more prominent as shown in Fig. 9a and b. At the right end of the contact interface, the maximum normal contact traction obtained by LC-RPIM is 1–1.5% lower compared to that of ABAQUS. The maximum value and region of the tangential relative slip decrease with the increase of the adhesion as shown in Fig. 9c. Next, in the absence of adhesion, Fig. 10 plots the contact stress and tangential relative slip along the contact interface with the change of its frictional coefficient. It is shown again that the numerical results of LC-RPIM are in good agreement with those of ABAQUS. With the increase of the frictional coefficient, the concentration of contact stress is significantly intensified as shown in Fig. 10a and b, but the maximum relative slip value and slip region decrease as shown in Fig. 10c. Note that the tangential relative slip of the contact interface decreases with the increase of the tangential adhesion and frictional coefficient.

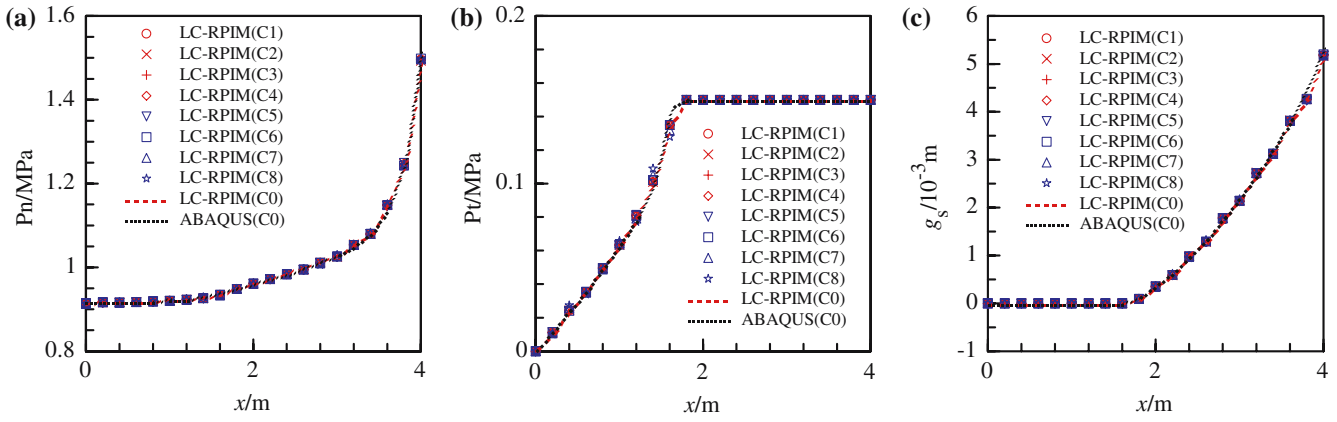

Fig. 11 Effect of the dimension of nodal local support domain, shape parameters in MQ-RBF and nodal irregularity for the contact of a rigid body located under an elastic body ($a_n = 0$, $a_s = 0.15$ MPa, $\mu = 0$). **a** Contact pressure. **b** Contact shear stress. **c** Tangential relative slip

5.1.3 Effect of the nodal local support domain, nodal irregularity and shape parameters

In this investigation, 441 field nodes is used, mechanical parameters of the contact interface are fixed at $a_s = 0.15$ MPa and $\mu = 0$. Figure 11 illustrates the contact stress and tangential relative slip obtained using ABAQUS and the proposed method for different parameters listed in Table 1. It is obvious that the numerical results of LC-RPIM agree well with those of ABAQUS. The proposed method is very stable, and its numerical results are independent of the dimension of nodal local support domain, nodal irregularity and shape parameters used in MQ-RBF.

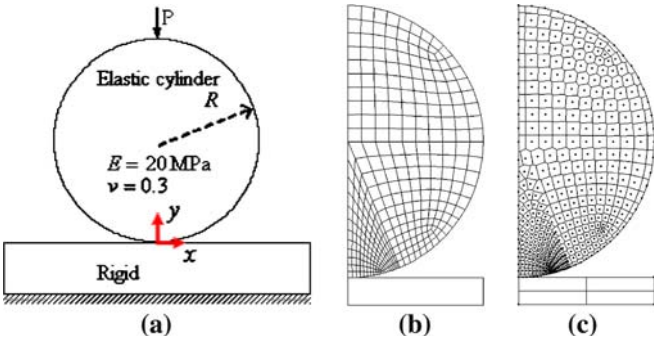

Fig. 12 Contact of a cylinder on a rigid body. A uniform pressure is applied at the top. **a** Mechanical configuration. **b** FE mesh. **c** Voronoi cells

5.2 Frictionless contact of an elastic cylinder on a rigid body

Consider now an infinitely long elastic cylinder in contact with a rigid body, as shown in Fig. 12a. The plane strain problem is considered. Only the right half is investigated because of its symmetry about y axis. FE mesh used for ABAQUS and Voronoi cells used for LC-RPIM are, respectively, shown in Fig. 12b and c. Material parameters of the cylinder are $E = 20$ MPa and $\nu = 0.3$. For the frictionless contact that the contact interface is perfectly smooth ($\boldsymbol{a} = 0$ and $\mu = 0$), by means of referencing the contact of two same elastic cylinders with identical mechanical parameters, the analytical solution can be obtained in terms of the contact length and contact pressure as given in [1]

$$l_c = 2\sqrt{\mathrm{P}(1-\nu^2)/(\pi E)} \tag{5.2}$$

$$\mathrm{P}n = P_0\sqrt{1-\left(x/l_c\right)^2} \tag{5.3}$$

where l_c and Pn are the potential contact area and pressure, respectively; $P_0 = 2P/(\pi l_c)$ is the maximum contact pressure and P is the uniform pressure per unit length along the longitudinal direction.

In this investigation, the nodal local support domain and shape parameters of Case C0 in Table 1 are used for MQ-RBF. Three loadings are used: P1 = 1.0 MPa, P2 = 1.5 MPa and P3 = 2.0 MPa. Contact pressure along the contact interface and horizontal displacement of the cylinder at the bottom obtained by the two methods are plotted in Fig. 13. It is shown that contact pressures obtained using the proposed LC-RPIM and ABAQUS are basically in good agreement with the analytical solutions, and the relative errors of the maximum contact pressure of both LC-RPIM and ABAQUS increase slightly with the magnitude of the loading as listed in Table 2. The contact areas obtained by both LCRPIM and ABAQUS are the same and their relative errors decrease with the increase of load as listed in Table 3.

5.3 Contact of an elastic square plate with circular hole sandwiched by two elastic plates

Consider a solid system composed of three elastic bodies, in which a square plate with circular hole is sandwiched by two identical plates, as shown in Fig. 14. The dimensions of these three bodies, applied pressure and material parameters

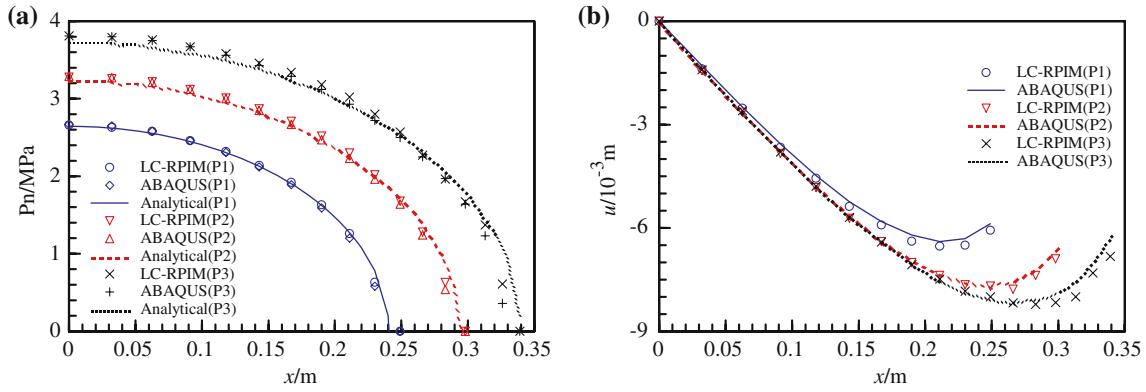

Fig. 13 Effect of load magnitude. Frictionless contact of a cylinder on a rigid body ($\alpha_s = 2.5$, $\alpha_c = 0.1$, $q = 1.05$, $\boldsymbol{a} = 0$, $\mu = 0$). **a** Contact pressure. **b** Horizontal displacement of the cylinder at bottom

Table 2 The maximum contact pressure and relative error for different methods and loads

Case	The maximum contact pressure P_0/MPa			Relative errors (%)	
	Analytical	ABAQUS	LCRPIM	ABAQUS	LCRPIM
P1	2.65	2.67	2.66	0.754717	0.377358
P2	3.24	3.29	3.28	1.54321	1.234568
P3	3.74	3.81	3.81	1.871658	1.871658

Table 3 The contact length and relative errors for different methods and loads

Case	The contact areas l_c/m			Relative errors (%)	
	Analytical	ABAQUS	LCRPIM	ABAQUS	LCRPIM
P1	0.241	0.249	0.249	3.319502	3.319502
P2	0.295	0.298	0.298	1.016949	1.016949
P3	0.340	0.339	0.339	−0.29412	−0.29412

used are also shown in Fig. 14. Because of its symmetry with respect to y axis, we only study the right part, and the plane stress problem is considered. The nodal local support domain and shape parameters of Case C0 in Table 1 are used in MQ-RBF.

5.3.1 Effect of the nodal density

In this investigation, the contact interfaces are set with the parameters of $\boldsymbol{a} = 0$ and $\mu = 0.5$. FE meshes used in ABAQUS and corresponding Voronoi cells used in LC-RPIM are shown in Fig. 15. The contact stress along the contact interfaces $\Gamma_{CI}^{(1)}$ and relative displacement along $\Gamma_{CI}^{(2)}$ are computed using the two methods and plotted in Figs. 16 and 17 for different nodal densities. It is shown that the proposed contact stresses basically agree well with those of ABAQUS. With the increase of the nodal density, the concentration of contact stress at the right end of the contact interface increases, accordingly whereas the actual contract area decreases. Note that the actual contact areas of the two contact interfaces are different under a given nodal density by comparing Figs. 16 and 17, which is caused by that the different constraint conditions that the bottom plate is fixed at the bottom and the top plate is subjected to a uniform pressure on the top. The relative displacements along the top contact interface obtained

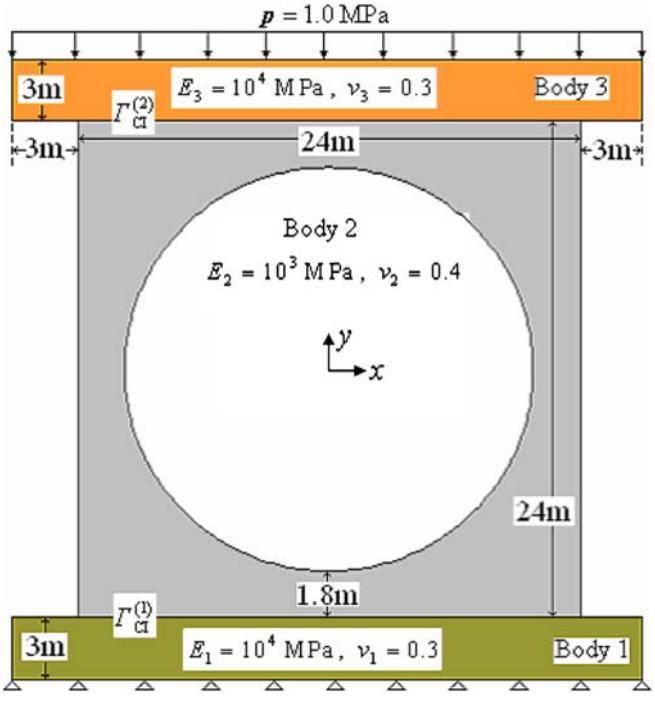

Fig. 14 Contact of an elastic square plate with circular hole sandwiched by two identical elastic plates. The top plate is subjected to a uniform pressure

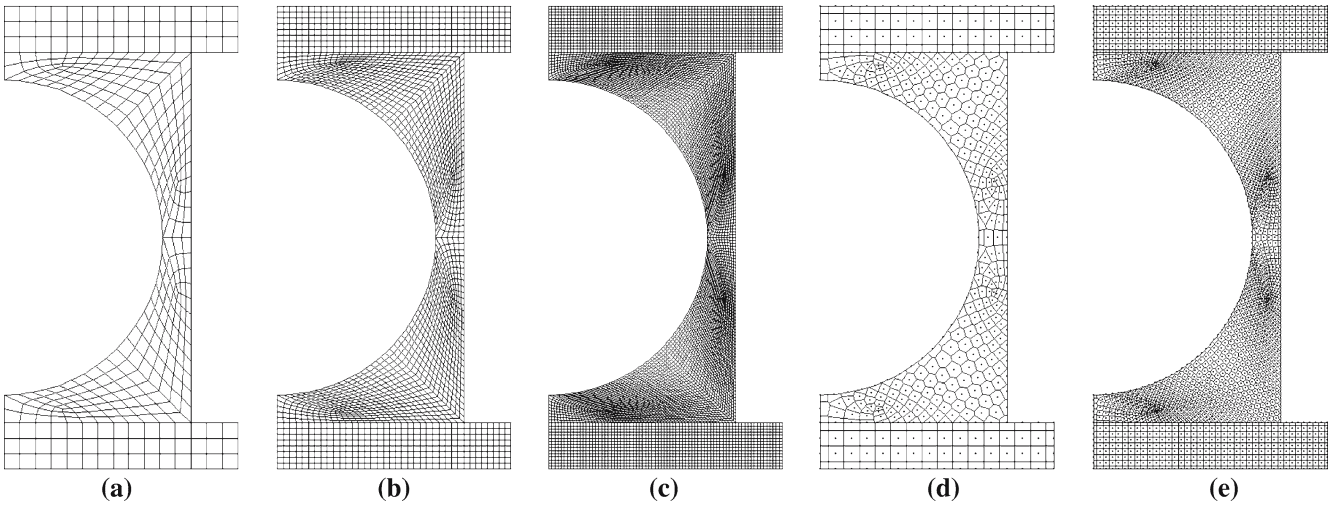

Fig. 15 Different nodal arrangement. The contact of an elastic square plate with circular hole sandwiched by two identical elastic plates. **a** FE Mesh for M1: $316 + 2 \times 64$ nodes. **b** FE mesh for M2: $1662 + 2 \times 351$ nodes. **c** FE mesh for M3: $6435 + 2 \times 1216$ nodes. **d** Voronoi cells for M1. **e** Voronoi cells for M2

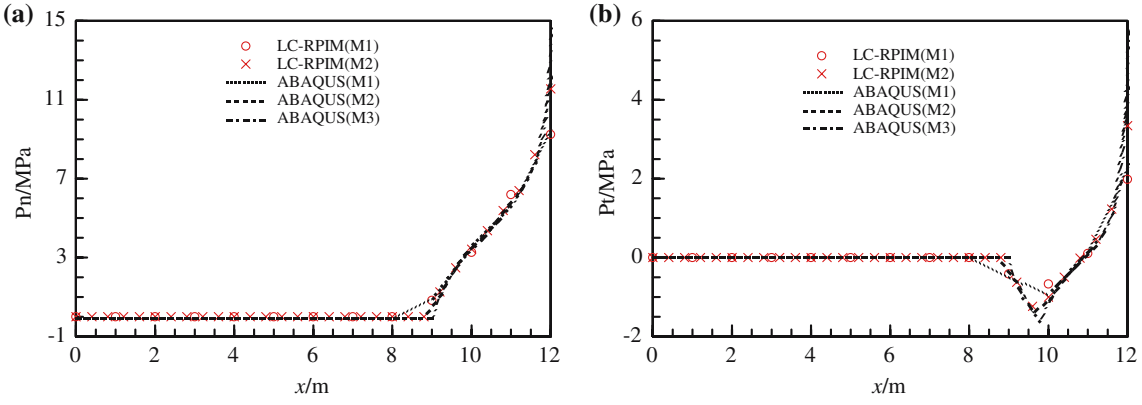

Fig. 16 Effect of nodal density on contact stress along $\Gamma_{\mathrm{CI}}^{(1)}$. The contact of an elastic square plate with circular hole sandwiched by two identical elastic plates ($\alpha_{\mathrm{s}} = 2.5$, $\alpha_{\mathrm{c}} = 0.1$, $q = 1.05$, $\boldsymbol{a} = 0$, $\mu = 0.5$). **a** contact pressure. **b** contact shear stress

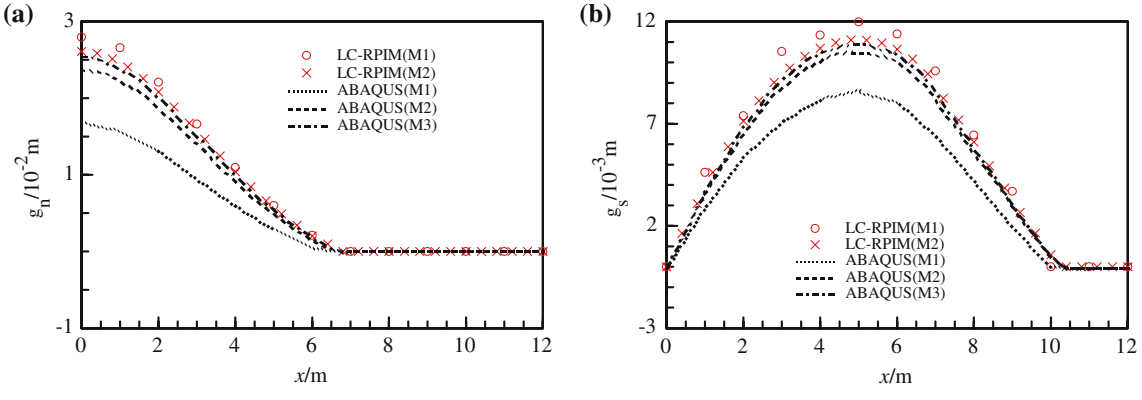

Fig. 17 Effect of nodal density on gap along $\Gamma_{\mathrm{CI}}^{(2)}$. The contact of an elastic square plate with circular hole sandwiched by two identical elastic plates ($\alpha_{\mathrm{s}} = 2.5$, $\alpha_{\mathrm{c}} = 0.1$, $q = 1.05$, $\boldsymbol{a} = 0$, $\mu = 0.5$). **a** Normal gap. **b** Tangential slip

using both methods are dependent on the nodal density. Figure 17 indicates that the numerical results of relative displacement of the top contact interface obtained by LC-RPIM approach the exact solution from above. However, those by ABAQUS approach the exact solution from below. The relative displacements of LC-RPIM for nodal density M3 are

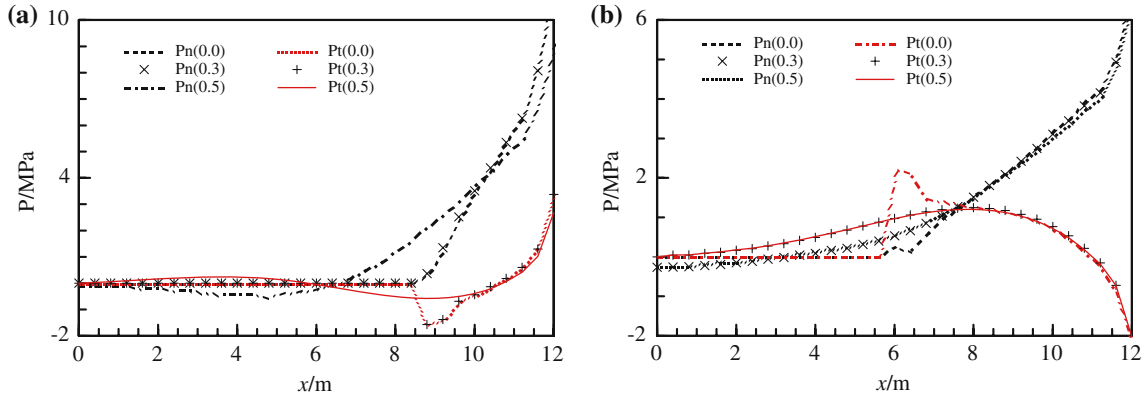

Fig. 18 Effect of the normal adhesion on contact stress. The contact of an elastic square plate with circular hole sandwiched by two identical elastic plates ($\alpha_s = 2.5$, $\alpha_c = 0.1$, $q = 1.05$, $a_s = 10\,\text{MPa}$, $\mu = 0$). **a** Contact stress along $\Gamma_{CI}^{(1)}$. **b** Contact stress along $\Gamma_{CI}^{(2)}$

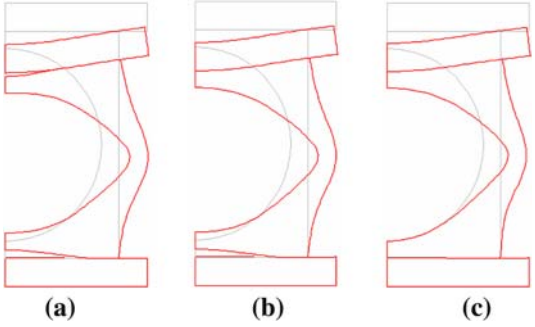

Fig. 19 Effect of the normal adhesion on deformation. The contact of an elastic square plate with circular hole sandwiched by two identical elastic plates ($\alpha_s = 2.5$, $\alpha_c = 0.1$, $q = 1.05$, $a_s = 10\,\text{MPa}$, $\mu = 0$). **a** $a_n = 0$. **b** $a_n = 0.3\,\text{MPa}$. **c** $a_n = 0.5\,\text{MPa}$

basically in accordance with those of ABAQUS for nodal density M4.

5.3.2 Effect of the normal adhesion

In the present study, nodal density M3 shown in Fig. 15g is used for LC-RPIM. $a_s = 10\,\text{MPa}$ and $\mu = 0$ are fixed for the two contact interfaces, and other parameters used are listed in Table 1 (Case C0). The numerical contact stress along the two contact interfaces are plotted in Fig. 18 while the normal adhesion varies. With the increase of the adhesion, the concentrations of contact stresses along the two contact interfaces decrease. The top and bottom contact interfaces adhere together from partly to fully step by step as shown in Fig. 19.

5.4 Contacts among three elastic bodies

Finally consider a solid system composed of two elastic bodies with initial gap in contacting on an elastic body, and their dimensions are shown in Fig. 20a. The bottom body is represented as $B^{(1)}$ with the material parameters of $E_1 = 10,000\,\text{MPa}$ and $\nu_1 = 0.3$. The two top bodies are denoted as $B^{(2)}$ and $B^{(3)}$ with an initial gap of $\delta = 0.002\,\text{m}$, and their material parameters are $E_2 = 5,000\,\text{MPa}$, $\nu_2 = 0.35$, $E_3 = 3,000\,\text{MPa}$, and $\nu_3 = 0.4$. In the system there are three contact interfaces with notations of $\Gamma_{CI}^{(1)}$, $\Gamma_{CI}^{(2)}$ and $\Gamma_{CI}^{(3)}$ as shown in Fig. 20a. In the absence of the adhesion, their frictional coefficients are 0.7, 0.5 and 0.3, respectively. The plane strain problem is considered. The applied pressures are $P_x = 2\,\text{MPa}$ and $P_y = 5\,\text{MPa}$. The FE mesh for ABAQUS and Voronoi cells for LC-RPIM are plotted in Fig. 20b and c, respectively. Other parameters used for LC-RPIM are listed in Table 1 (Case C0).

Numerical results obtained using the two methods are plotted in Fig. 21. It is shown that the contact stresses along the three contact interfaces of LC-RPIM are in good agreement with those of ABAQUS as shown in Fig. 21a, b and c. In addition, the deformations of the bottom body along its top surface obtained by LC-RPIM also agree well with those by ABAQUS as shown in Fig. 21d. It is indicated that the present method works well for asymmetric contact problems.

6 Conclusions

In this paper, a numerical approach using LC-RPIM is presented for 2D contact analysis of a solid system which is composed of rigid and deformable solids (or bodies). A modified Coulomb frictional contact model considering the normal adhesion for tensile and tangential adhesion for slipping is introduced and its discretized form is given out by contact point-pairs for a contact interface. A subdomain parametric variational principle in incremental form of the potential energy is used to construct the governing equation based on the virtual work principle. The final discretized system equations are transformed to a standard form of linear complementarity problem (LCP). The present approach can

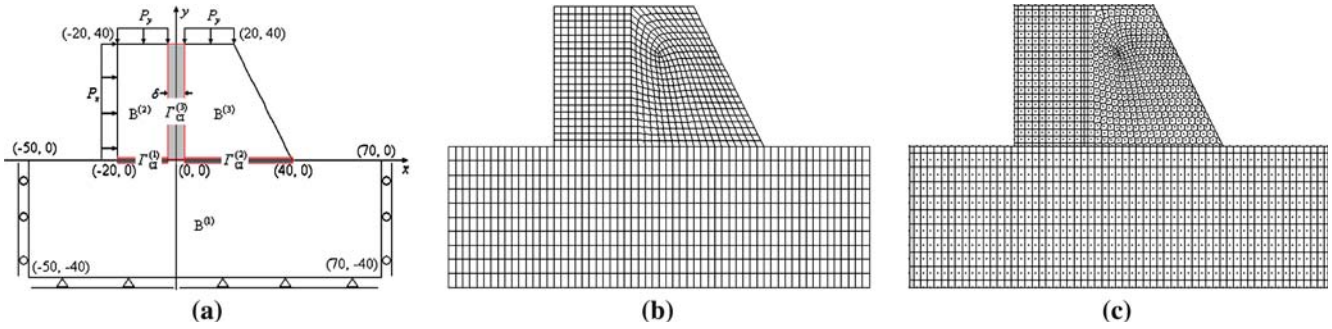

Fig. 20 Contacts among three elastic bodies. **a** Configuration (all dimensions in meters). **b** FEM mesh for ABAQUS. **c** Voronoi cells for LC-RPIM

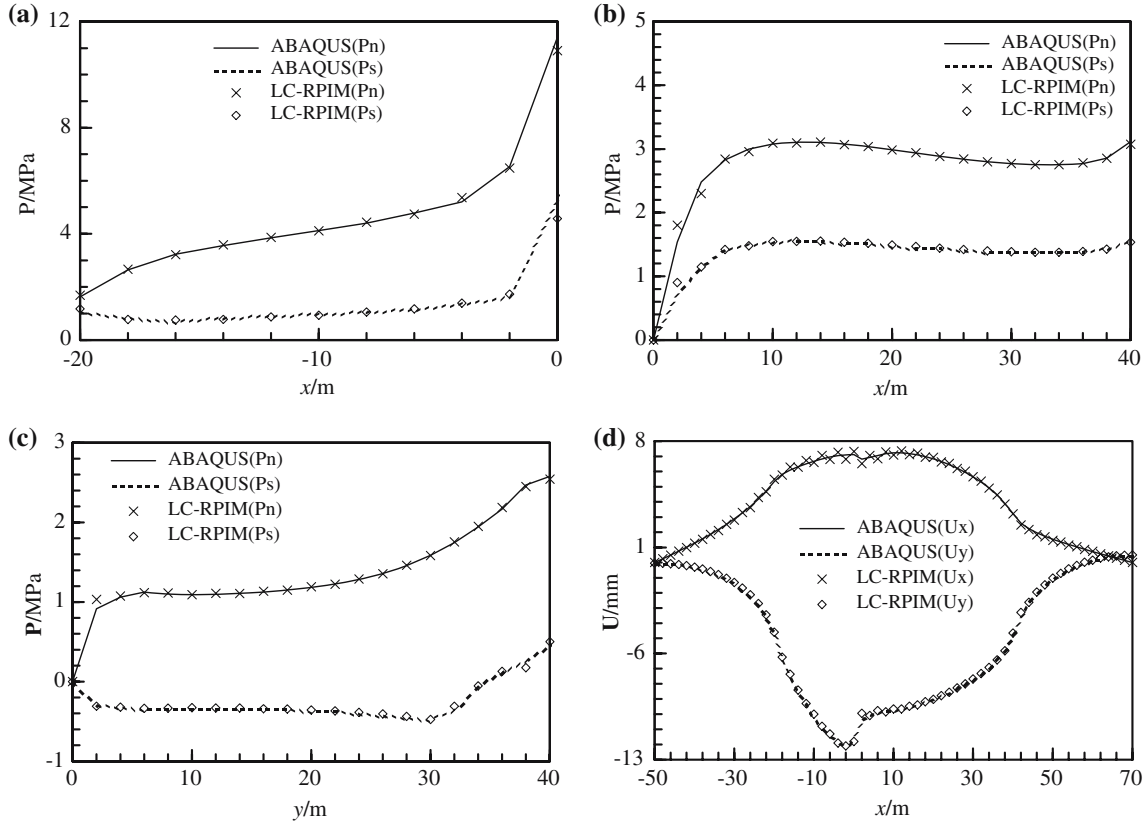

Fig. 21 Numerical results obtained by using the present method and ABAQUS for the contacts among three elastic bodies. **a** Contact stress along $\Gamma_{\mathrm{CI}}^{(1)}$. **b** Contact stress along $\Gamma_{\mathrm{CI}}^{(2)}$. **c** Contact stress along $\Gamma_{\mathrm{CI}}^{(3)}$. **d** Displacement along the top surface of body 1

well simulate the behavior of contact nonlinearity including contact/departing or adhesion/debonding, and sticking/slipping among the potential contact interfaces in a solid system.

By comparison with ABAQUS or analytical solution via several numerical examples, it can be concluded that the proposed method yields accurate and stable solution regardless of the dimension of the local support domain, nodal irregularity and shape parameters used in MQ-RBF. The method works well for both symmetric and asymmetric contact problems.

References

1. Kikuchi N, Oden JT (1988) Contact problem in elasticity: a study of variational inequalities and finite element methods. SIAM, Philadelphia
2. Wriggers P (2002) Computational contact mechanics. Wiley, Hoboken
3. Nour-omid B, Wriggers P (1987) A note on the optimum choice for penalty parameters. Commun Appl Numer Methods 3:581–585
4. Pusoa MA, Laursen TA (2004) A mortar segment-to-segment contact method for large deformation solid mechanics. Comput Methods Appl Mech Eng 193:601–629

5. Wriggers P, Zavarise G (1997) On contact between three-dimensional beams undergoing large deformations. Commun Numer Methods Eng 13:429–438
6. Talon C, Curnier A (2003) A model of adhesion coupled to contact and friction. Eur J Mech A/Solids 22:545–565
7. Papadopolos P, Solberg JM (1998) A Lagrange multiplier method for the finite element solution of frictionless contact problems. Methods Comput Modelling 28:373–384
8. Wriggers P, Zavarise G (1993) Application of augmented Lagrangian techniques for non-linear constitutive laws in contact interfaces. Commun Num Methods Eng 9:815–824
9. Simo JC, Laursen TA (1992) An augmented Lagrangian treatment of contact problems involving friction. Comput Struct 42:97–116
10. Pietrzak G, Curnier A (1996) Large deformation frictional contact mechanics: continuum formulation and augmented Lagrangian treatment. Comput Methods Appl Eng 177:351–381
11. Chabrand P, Dubois F, Raous M (1998) Various numerical methods for solving unilateral contact problems with friction. Mathods Comput Modelling 28(4–8):97–108
12. Klarbring A (1999) Contact, friction, discrete mechanical structures and mathematical programming. In: Wriggers P, Panagiotopoulos P (eds) New developments in contact problems. Springer, Berlin Heidelberg New York, pp 55–100
13. Raous M (1999) Quasistatic Signorini problem with Coulomb friction and coupling to adhesion. In: Wriggers P, Panagiotopoulos P (eds) New developments in contact problems. Springer, Berlin Heidelberg New York, pp 101–178
14. Wriggers P, Haraldsson A (2003) A simple formulation for two-dimensional contact problems using a moving friction cone. Commun Num Methods Eng 19:285–295
15. Zavarise G, Wriggers P, Schrefler BA (1998) A method for solving contact problems. Int J Num Methods Eng 42:473–498
16. Kane C, Repetto EA, Ortiz M, Marsden JE (1999) Finite element analysis of nonsmooth contact. Comput Methods Appl Mech Eng 180:1–26
17. Pandofi A, Kane C, Marsden JE, Ortiz M (2002) Time-discretized variational formulation of non-smooth frictional contact. Int J Numer Methods Eng 53:1801–1829
18. Olukoko OA, Becker AA, Fenner RT (1993) Independent meshing of contacting surfaces using fictitious nodes in boundary element analysis. Comput Struct 48:787–801
19. Dostal Z, Friedlander A, Santos SA, Malik J (1996) Analysis of semicoercive contact problems using symmetric BEM and augmented Lagrangians. Eng Anal Bound Elem 18:195–201
20. Leahy JG and Becker AA (1999) The numerical treatment of local variables in three-dimensional frictional contact problems using the boundary element method. Comput Struct 71:383–395
21. Gun H (2004) Boundary element analysis of 3-D elasto-plastic contact problems with friction. Comput Struct 82:555–566
22. Cundall PA, Strack ODL (1979) A discrete numerical model for granular assemblies. Geotech 29:47–65
23. Fortin J, Hjiajb M, Saxce GD (2002) An improved discrete element method based on a variational formulation of the frictional contact law. Comput Geotech 29:609–640
24. Shi GH (1988) Discontinuous deformation analysis – a new numerical model for the statics, dynamics of block systems (Ph.D. thesis). Univ. California, Berkeley, USA
25. Cheng YM (1998) Advancements and improvement in discontinuous deformation analysis.Comput Geotech 22:153–163
26. Li Y (2000) Discontinuous deformation computational mechanic model and its applications in geotechnical engineering (Ph.D. thesis). Dalian univ Tech, Dalian, PRC (in Chinese)
27. Li Y, Luan MT (2000) Fundamentals and formulations of discontinuous deformation mechanics model and its linear programming algorithm. J Dalian Univ Tech 40:351–357 (in Chinese)
28. Liu GR (2003) Meshfree methods: moving beyond the finite element method. CRC Press, Boca Raton
29. Liu GR, Gu Y T (2005) An introduction to meshfree methods and their programming. Springer, Berlin Heidelberg New York
30. Lucy LB (1977) A numerical approach to the testing of fusion process. J Astron 88:1013–1024
31. Gingold RA, Monaghan JJ (1977) Smoothed particle hydrodynamics: theory and application to non-spherical stars. Mon Not R Astron Soc 181:375–389
32. Randles PW, Libersky LD (1996) Smoothed particle hydrodynamics: some recent improvements and applications. Comput Methods Appl Mech Eng 139:375–408
33. Liu GR, Liu MB (2003) Smoothed particle hydrodynamics: a meshfree particle method. World Scientific, New Jersey
34. Belytschko T, Lu YY, Gu L (1994) Element-free Galerkin methods. Int J Num Methods Eng 37:229–256
35. Lu Y, Belytschko T, Gu L (1994) A new implementation of the element-free Galerkin method. Comput Methods Appl Mech Eng 133:397–414
36. Belytschko T, Krongauz Y, Organ D, Fleming M, Krysl P (1996) Meshless methods: an overview and recent developments. Comput Methods Appl Mech Eng 137:3–47
37. Liu WK, Jun S, Zhang YF (1995) Reproducing kernel particle methods. Int J Num Methods Fluids 20:1081–1106
38. Atluri SN, Zhu T (1998) A new meshless local Petrov–Galerkin (MLPG) approach in computational mechanics. Comput Mech 22:117–127
39. Atluri SN, Cho JY, Kim HG (1999) Analysis of the thin beam, using the meshless local Petrov–Galerkin (MLPG) method, with generalized moving least squares interpolations. Comput Mech 24: 334–347
40. Liu GR, Gu YT (2000) Meshless local Petrov-Galerkin (MLPG) method in combination with finite element and boundary element approaches. Comput Mech 26:536–546
41. Liu GR, Gu YT (2001) A point interpolation method for two-dimensional solid. Int J Num Methods Eng 50:937–951
42. Wang JG, Liu GR, Lin P (2002) Numerical analysis of Biot's consolidation process by radial point interpolation method. Int J Solids Struct 39:1557–1573
43. Wang JG, Liu GR (2002) On the optimal shape parameters of radial basis functions used for 2-d meshless methods. Comput Methods Appl Mech Eng 191:2611–2630
44. Dai KY, Liu GR, Lim KM, Gu YT (2003) Comparison between the radial point interpolation and the Kriging based interpolation used in meshfree methods. Comput Mech 32:60–70
45. Liu GR, Dai KY, Han X, Li Y (2006) A meshfree minimum length method for 2-D problems. Comput Mech (in press)
46. Liu GR, Li Y, Luan MT, Dai KY, Xue W (2005) A linearly conforming radial point interpolation method (RPIM). ICMR, AKITA
47. Liu GR, Li Y, Luan MT, Dai KY, Xue W (2006) A linearly conforming radial point interpolation method for solid mechanics problems. Int J Comput Methods
48. Chen JS, Wu CT, Yoon S, You Y (2001) A stabilized conforming nodal integration for Galerkin mesh-free methods. Int J Num Methods Eng 50:435–466
49. Chen JS, Yoon S, Wu CT (2002) Non-linear version of stabilized conforming nodal integration for Galerkin mesh-free methods. Int J Num Methods Eng 53:2587–2615
50. Belytschko T, Fleming M (1999) Smoothing, enrichment and contact in the element-free Galerkin method. Comput Struct 71: 173–195
51. Xiao JR, Gamaa BA, Gillespie JW, Kansad EJ (2005) Meshless solutions of 2D contact problems by subdomain variational inequality and MLPG method with radial basis functions. Eng Anal Bound Elem 29:95–106.
52. Powell MJD (1992) The theory of radial basis function approximation in 1990. In: Light FW (ed) Advances in numerical analysis. Oxford University Press, Oxford, pp 303–322
53. Golberg MA, Chen CS, Karur SR (1996) Some recent results and proposals for the use of radial basis functions in the BEM. Eng Anal Bound Elem 18:9–17
54. Dineen S (1998) Multivariate calculus and geometry. Springer, Berlin Heidelberg New York
55. Hardy RL (1990) Theory and applications of the multiquadrics–biharmonic method (20 years of discovery 1968–1988). Comput Mathods Appl 19:163–208

56. Bonet J, Kulasegaram S (2002) A simplified approach to enhance the performance of smooth particle hydrodynamics methods. Appl Mathods Comput 126:133–155
57. Curnier A (1999) Unilateral contact: mechanical modelling. In: Wriggers P, Panagiotopoulos P (eds) New developments in contact problems. Springer, Berlin Heidelberg New York, pp 1–54
58. Curnier A (1983) A theory of friction. Int J Solids Struct 20: 637–647
59. Zhong WX, Zhang RL (1988) Parametric variational principles and their quadratic programming solutions in plasticity. Comput Struct 30:887–896
60. Zhang HW, Zhang XW, Chen JS (2003) A new algorithm for numerical solution of dynamic elastic–plastic hardening and softening problems. Comput Struct 81:1739–1749
61. Cottle RW, Pang JS, Stone RE (1992) The linear complementarity problem. Academic, Boston